

# 1 Estimation of mud and sand fractions and total concentration from coupled 2 optical-acoustic sensors

3 Duc Tran<sup>1,3</sup>, Matthias Jacquet<sup>1</sup>, Stuart Pearson<sup>2</sup>, Bram Van Prooijen<sup>2</sup> and Romaric Verney<sup>1</sup>

4 <sup>1</sup> IFREMER, DYNECO/DHYSED, ZI pointe du Diable, CS10070 Plouzane, France

5 <sup>2</sup> Faculty of Civil Engineering and Geosciences, Delft University of Technology, P.O. Box 5048,  
6 2600GA, Delft, the Netherlands

7 <sup>3</sup> Current: Royal Belgian Institute of Natural Sciences, OD Nature, Rue Vautier 29, 1000  
8 Brussels, Belgium

## 9 ABSTRACT

10 Optical and acoustic sensors have been widely used in laboratory experiments and field stud-  
11 ies to investigate suspended particulate matter concentration and particle size over the last  
12 four decades. Both methods face a serious challenge as laboratory and in-situ calibrations are  
13 usually required. Furthermore, in coastal and estuarine environments, the coexistence of mud  
14 and sand often results in multimodal particle size distributions, amplifying erroneous mea-  
15 surements. This paper proposes a new approach of combining a pair of optical-acoustic sig-  
16 nals to estimate the total concentration and sediment composition of a mud/sand mixture in  
17 an efficient way without an extensive calibration. More specifically, we first carried out a set of  
18 54 bimodal size regime experiments to derive empirical functions of optical-acoustic signals,  
19 concentrations, and mud/sand fractions. The functionalities of these relationships were then  
20 tested and validated using more complex multimodal size regime experiments over 30 optical-  
21 acoustic pairs of 5 wavelengths (420, 532, 620, 700, 852 *nm*) and 6 frequencies (0.5, 1, 2, 4, 6,  
22 8 *MHz*). In the range of our data, without prior knowledge of particle size distribution, com-  
23 binations between optical wavelengths 620-700 *nm* and acoustic frequencies 4-6 *MHz* predict  
24 mud/sand fraction and total concentration with the variation < 10% for the former and < 15%

---

email addresses: dtran@naturalsciences.be (Duc Tran), romaric.verney@ifremer.fr (Romaric Verney)

25 for the later. This approach therefore enables the robust estimation of suspended sediment  
26 concentration and composition, which is particularly useful in cases where calibration data is  
27 insufficient.

28 **Keywords:**

29 Acoustic, Optical, Sand, Mud, SPM concentration, DEXMES,

30 **1 INTRODUCTION**

31 Accurate observation of suspended particulate matter concentration (SPMC) typically requires  
32 combinations of one or more optical and acoustic sensors with gravimetric measurements of  
33 filtered water samples (Sutherland et al., 2000; Bux et al., 2019; Fettweis et al., 2019). This is be-  
34 cause both optical and acoustic sensors indirectly measure either the attenuation/backscattered  
35 signal of an optical beam or the acoustic backscatter as a proxy of SPMC. Conversely, the gravi-  
36 metric measurements of filtered water samples directly provide the ground truth reference of  
37 SPMC. A regression model is then developed based on these indirect measurements and di-  
38 rect measurements of SPMC (Fettweis et al., 2019). Both direct or indirect measurements of  
39 SPMC have their own drawbacks. Physical water sampling is often impractical and expen-  
40 sive, particularly at high-frequencies over long periods for timeseries or vertical profile data  
41 collections. Optical and acoustic methods, on the other hand, provide high-resolution mea-  
42 surements. However, these two methods demand laboratory and *in-situ* calibration owing to  
43 the strong dependence of the backscattering characteristics on mineralogical compositions,  
44 particle size, density and shape (Slade et al., 2011; Salehi and Strom, 2011; Doxaran et al., 2016;  
45 Druine et al., 2018). The backscattering signal is also influenced by the presence of salinity,  
46 bubbles and biological fouling (Downing, 2006; Salehi and Strom, 2011; Sahin et al., 2017; Bux  
47 et al., 2019; Haalboom et al., 2021). In practice, optical and acoustic measurements often com-  
48 bine with several *in-situ* or laboratory calibrations of water samples obtained from the field.  
49 For reliable and high fidelity data, it is suggested that sensors need to be re-calibrated with wa-

50 ter samples when there are significant changes in SPM compositions and/or hydrodynamics  
51 conditions (Moura et al., 2011; Fettweis et al., 2019; Pearson et al., 2021; Haalboom et al., 2021).  
52 Hence, these methods require not only site-specific but also instrument-specific calibrations,  
53 adding another layer of difficulty and uncertainty to the inversion process.

54 Particles in suspension respond to both optical and acoustic signals via a similar mech-  
55 anism, albeit to different degrees. Optical sensors illuminate a water sample volume with a light  
56 source, then the photodetectors convert either the optical beam attenuation or back(side)scatter  
57 intensity of the light in voltage or turbidity units (Downing, 2006; Fettweis et al., 2019). Similarly,  
58 acoustic sensors indirectly estimate concentration by quantifying the changes in backscattered  
59 acoustic signals, in  $dB$  (Sahin et al., 2017; Bux et al., 2019; Haalboom et al., 2021). The peak sen-  
60 sitivity of acoustic backscatter signal to particle size occurs at upper limit of the Rayleigh regime  
61 at  $2\pi r \lambda^{-1} \approx 1$  (Downing, 2006; Thorne and Hurther, 2014; Haalboom et al., 2021), where  $r$  is the  
62 particle radius and  $\lambda$  is the acoustic wavelength. For example, an Acoustic Doppler Velocimeter  
63 (ADV) working at 2 or 6  $MHz$  will have the best performance with sand particles at sizes of 240  
64 or 80  $\mu m$ , respectively. For optical backscatter sensors, the light scattering and refractive index  
65 are largely dictated by the number of illuminated particles, or total illuminated areas (Downing,  
66 2006), hence, the optical sensors are more sensitive to finer particles, i.e., mud ( $d_{50} < 63 \mu m$ ). If  
67 we combine both optical and acoustic sensors in one measurement of the same suspension we  
68 would thus “see” the mud better and “hear” the sand better. This allows us to gain deeper un-  
69 derstanding about the suspension than we could if we only use a single type of sensor (Pearson  
70 et al., 2021; Livsey et al., 2023).

71 This study focuses on proposing a new method to use coupled optical-acoustic measure-  
72 ments to infer SPM compositions and concentrations without or with limited water sampling  
73 calibrations. As discussed above, optical backscattering signals are highly sensitive to mud, and  
74 acoustic backscattering signals are highly sensitive to sand particles, and vice versa. We further  
75 hypothesize that SPMC and composition can be differentiated and calculated based on such  
76 sensitivities and differences in behaviors of mud and sand to different types of signals, i.e., op-

77 tical and acoustic. The first objective of this paper is to investigate the possibility of combining  
78 a pair of optical and acoustic sensors to provide information about the mud/sand fraction and  
79 SPMC. To do so, we will quantify the sensitivity of a wide range of commercially available optical  
80 and acoustic sensors to the evolution of suspensions from mud-dominant to sand-dominant  
81 settings. More specifically, five optical and acoustic sensors will be used to cover the wave-  
82 lengths from 420 to 852  $nm$  and frequencies from 0.5 to 8  $MHz$ , resulting in 30 different pairs  
83 of one wavelength and one frequency for each experiment. The second objective is to quantify  
84 at which wavelength/frequency the pair of optical and acoustic sensors will provide the most  
85 accurate estimation of SPMC at given concentration and particle size characteristics.

## 86 2 EXPERIMENTAL SETUP AND DATA PROCESSING

### 87 2.1 Experimental setup

88 Two sets of experiments were conducted to test and validate the hypothesis. The first set, the  
89 Calibration set ( $C_{set}$ ) consisting of 54 experiments, was examined to derive empirical relation-  
90 ships between each pair of optical/acoustic signal and mud/sand fraction ( $f_{mud}$ ) and concen-  
91 tration. The second set, the Validation set ( $V_{set}$ ) used 6 experiments to justify the applicability  
92 of such empirical relationships in predicting  $f_{mud}$  and SPMC of the suspension.

93 Table 1 shows the experimental conditions in  $C_{set}$ . In this study, Bentonite and two par-  
94 ticle sizes of sand were utilized to represent mud and sand. The sands were sieved with sieve  
95 mesh 100 – 125  $\mu m$  and 200 – 250  $\mu m$  to obtain sand S1 ( $d_{50} = 110 \mu m$ ) and S2 ( $d_{50} = 240 \mu m$ ),  
96 respectively. Five ratios of mud/sand fractions,  $f_{mud}$ , were investigated: pure Bentonite ( $f_{mud}$   
97 = 100%), pure sand ( $f_{mud} = 0\%$ ), and three intermediate mixtures: 75, 50, 25%. Hereafter, the  
98 suffixes 1 and 2 refer to the sand particle sizes of S1 ( $d_{50} = 110 \mu m$ ) and S2 ( $d_{50} = 240 \mu m$ ), re-  
99 spectively. The suffixes \_100, \_75, \_50, \_25, \_0 refer to the fraction of Bentonite in suspension,  
100 or  $f_{mud}$ . For example, C1\_75 indicates the experiment from calibration set,  $C_{set}$ , in which the  
101 suspension consists of Bentonite and sand S1 with the ratio of mud/sand,  $f_{mud}$ , is 75%. For  
102 each SPM content condition, 6 concentrations were tested stepwise from 15 to 200  $mg/L$  (Table

103 1). We processed the data from  $C_{set}$  as three populations which are 1) **C1**: pure Bentonite and  
104 all S1-related experiments 2) **C2**: pure Bentonite and all S2-related experiments and 3) combi-  
105 nation of C1 and C2 called **C12**. In this study, there was only one pure Bentonite experiment;  
106 however, for consistency it was referred as C1\_100 in C1 and C2\_100 in C2, respectively.

107 Table 2 provides details of 6 additional experiments in  $V_{set}$ . It is noted that while  $C_{set}$  is a  
108 bimodal particle size mixture,  $V_{set}$  is a multimodal particle size mixture. In fact,  $V_{set}$  was split  
109 in a way that either Bentonite, S1, or S2 was the dominant sediment in various mixture ratios  
110 among the three types of sediments at least once. Thus, results from  $V_{set}$  provide not only a  
111 higher range of concentrations but also an expanded range of  $f_{mud}$ . In Table 2, the numbers  
112 outside the parentheses refers to the targeted concentrations or Bentonite fraction,  $f_{mud}$ . The  
113 numbers inside the parentheses refer to the true values of the parameters. These numbers were  
114 often less than the targeted concentrations because the applied turbulent shear was not high  
115 enough to keep all the sand in suspension at the elevation of the sensors, especially S2 ( $d_{50} =$   
116  $240 \mu m$ ).

117 Table 3 summarizes all the optical and acoustic sensors used in this study. Specifically,  
118 the sensors are HydroScat-4 with four channels 852, 620, 532, 420  $nm$ , Wetlabs\_FLNTU 700  
119  $nm$ , Laser In-Situ Scattering and Transmissometry - Acoustic Backscatter Sensor (LISST-ABS)  
120 8  $MHz$ , Nortek Vector Acoustic Doppler Velocimeter (ADV) 6  $MHz$ , AQUAscat-1000R with four  
121 transducers 4, 2, 1, and 0.5  $MHz$ . In this study, the sensors were setup so that the measuring  
122 volume of each sensor was at a similar level, around 26-33  $cm$  below the water surface (Fig. 1).

123 All experiments were conducted in the DEXMES tank, (Dispositif EXpérimental de quan-  
124 tification des Matières En Suspension), a novel device which was particularly designed for SPM  
125 experiments (Tran et al., 2021). DEXMES tank provides sufficient volume, approximately  $1 m^3$ ,  
126 for several sensors to function simultaneously. In general, the tank was filled with fresh water  
127 and left overnight to reach room temperature. An experiment was started with 30  $min$  of high  
128 shearing to remove bubbles inside the tank. In all experiments, the impeller was set at speed  
129 of 175 rotations per minute to provide high turbulent shear stress  $G = 30 - 100 s^{-1}$  in the tank

130 (Tran et al., 2021). For mud, Bentonite was stabilized in suspension for 30 *min* in a 5 *L* beaker  
131 with a mixer before being introduced into DEXMES. Next, a 30 *min* mixing was applied to pro-  
132 vide enough time for Bentonite particles to reach equilibrium. Then, sand was added to the  
133 DEXMES tank, 5 *min* before data collection, to reach the targeted concentration. At the end  
134 of the 10 *min* recording step, one 1 *L* water sample was collected using a nozzle located at  $\approx$   
135 25 *cm* below the water surface and 12 *cm* away from the wall of the tank. This procedure was  
136 repeated for all concentration levels (Table 1 and Fig. 1). In  $V_{set}$ , for better calibration of the  
137 true fractions of Bentonite, S1, and S2 in suspension instead of one 1 *L* water sample, three 1 *L*  
138 water samples were collected and analyzed.

## 139 **2.2 Data processing**

### 140 **2.2.1 Optical and acoustic signal**

141 All sensors started recording in real-time, continuous mode before any sediment was intro-  
142 duced into the tank until the last water sample was collected. For each examined condition,  
143 10 min data was averaged and utilized in the analysis (Table 1). Preliminary experiments sug-  
144 gested that the numbers of spike/bad data points are negligible. Hence, there was no further  
145 transformation and/or correction of the output signals, except for Wetlabs\_FLNTU where the  
146 output signal was converted from *count* to *NTU* as recommended by the Sea-Bird Scientific:  
147  $NTU = 0.0484(count - 50)$ . Another note is that the LISST-ABS is used with its default (fac-  
148 tory) concentration without calibration. Thus, even though the unit of the output from the  
149 LISST-ABS is *mg/L*, it is still “raw signal”. In the present paper, we consider each transducer  
150 of the AQUAscat-1000R and each channel of the HydroScat-4 as individual sensor (Table 3).  
151 It is also noted that due to the nature of signal recording mechanisms, the relationships of  
152 ADV (*SNR* – *dB*) signal and SPMC or optical signal is a log-linear. Hence, in order to pair with  
153 ADV signal the concentration or optical data is converted via a  $10\log_{10}()$  function (Hoitink and  
154 Hoekstra, 2005; Salehi and Strom, 2011; Chmiel et al., 2018). Regarding AQUAscat-1000R sensor,  
155 AQUATEC suggested to use a quadratic regression between concentration and the backscatter

156 signal (Eq. 4 – Aquatec Subsea Ltd (2012)). Subsequently, when pairing with optical or con-  
157 centration data, AQUAscat signal is transformed to  $AQUAscat_{signal}^2$ . The primary goal of this  
158 study is to investigate the behavior of optical/acoustic signals to different SPM concentrations  
159 and compositions. We have no intention to make a comparison between different commercial  
160 sensors, henceforth, the optical and acoustic sensors will be referred as their wavelengths or  
161 frequencies rather than by names or brands (last column in Table 3).

### 162 **2.2.2 Water sample**

163 For each  $V_{set}$  condition, three 1 L water samples were collected. S2, S1, and Bentonite are sepa-  
164 rated by sieving through 125 and 63  $\mu m$  sieves to obtain sand S2 and S1 on aluminum pans, and  
165 then filtered with a glass fiber filter to capture Bentonite, respectively. The separated sediments  
166 were dried in an oven at 50°C in 24 hours and then weighted to measure mass concentration.  
167 There are a few notes regarding water sample data. First, in  $C_{set}$ , there were only two types of  
168 sediment, Bentonite and either S1 or S2, therefore we did not separate mud/sand in quantify-  
169 ing total concentration in  $C_{set}$ . Rather, the fraction and concentration of S1 or S2 in  $C_{set}$  are  
170 acquired by subtracting the  $f_{mud}$  from the total concentration. Second, mass concentration  
171 data showed that the true values of concentration for Bentonite and sand S1 are 5-10% lower  
172 than the target values or some times even 40%, for S2. This is because 1) the turbulence in the  
173 tank was not high enough to keep all the sand in suspension, particularly S2 and 2) we later  
174 found that the mesh size of the glass fiber filter (0.7  $\mu m$ ) was slightly bigger than the smallest  
175 particle sizes of the clay (Table 2). This is the reason why  $f_{mud}$  and concentrations in C2 and  
176  $V_{set}$  cases were always noticeably different from the targeted values. Subsequently, for simplic-  
177 ity and convenience, the term  $f_{mud}$ , e.g., 100, 75, 50, 25, and 0%, actually refers to a very loose  
178 range, and sometimes even overlap, of mud/sand fraction, rather than indicating an absolute  
179 number. For example,  $f_{mud} = 75\%$  implies a range of  $f_{mud}$  from around 65 to 85% instead of  
180 exact 75%. Even without reaching exact targets, we still have a broad range representative of  
181 mud/sand-dominant environments. Third, mass concentrations from three 1 L water samples

182 in each  $V_{set}$  condition were almost the same (variations around 3%), verifying the quantifica-  
183 tion of  $f_{mud}$  in  $V_{set}$ . All calculations, data analysis, and figures are based on the true values  
184 of  $f_{mud}$ , mass of Bentonite, S1, and S2 in the mixture and total concentrations obtaining from  
185 physical water samples.

### 186 3 DERIVATION OF EMPIRICAL FUNCTIONS

187 In Pearson et al. (2021), we tested and validated a new concept, the Sediment Composition  
188 Index (SCI), in which the dynamics of mud/sand in suspension could be derived from optical  
189 and acoustic measurements, i.e.,  $SCI = 10 \log_{10}(OBS_{signal}) - ADV_{signal}$ . The present paper  
190 further develops the SCI concept, aiming to quantify mud/sand concentration. This section  
191 uses data from  $C_{set}$  to demonstrate how  $f_{mud}$  and total concentration can be obtained from  
192 one pair of raw optical and acoustic signals. First, only one pair of optical/acoustic signals is  
193 used for demonstration. Then, the application of the same procedure to all optical/acoustic  
194 pairs is discussed.

#### 195 3.1 Approach

196 The hypothesis under investigation is that because acoustic sensors are more sensitive to coarse  
197 sediments and optical sensors are more sensitive to mud, the sediment sensitivity differences  
198 can be used to elucidate the fraction of mud/sand in the mixture when both optical and acous-  
199 tic sensors are combined in one measurement. Figure 2 reveals the relationships of signal-  
200 signal and signal-concentration in  $C_{set}$ . For better illustrations and simplicity, data from one  
201 pair of optical/acoustic sensor, ( $O_{700} - A_8$ ), out of 30 pairs from C1 were used in Figure 2. Three  
202 observations can be made from this example. First, in Figure 2a,c,e pure mud (C1\_100) and pure  
203 sand (C1\_0) conditions are always the boundaries of mixed mud/sand conditions and lean to-  
204 ward the optical/acoustic axes, confirming that optical/acoustic sensors indeed respond better  
205 to finer/coarser sediments, respectively. Second, there is a linear relationship between signal-  
206 signal (Fig. 2a) and signal-concentration (Fig. 2c,e) of the same  $f_{mud}$ , e.g., five lines uniquely

207 associated with five mud/sand ratios  $f_{mud}$ . In other words, the signal magnitudes of both sen-  
 208 sors increase with the increase of concentration, yet the ratio of the optical/acoustic signal or  
 209 concentration/signal remains constant. Third, theoretically, all the lines should converge to  
 210 the point (0,0), which represents conditions with clear water, no turbulence shear, and no sed-  
 211 iment. This is essentially the case in our experiments. These observations suggest that there  
 212 are strong and unique relationships among raw signals, concentrations, and  $f_{mud}$ . This paper  
 213 adopted the Curve Fitting Tool, provided by Matlab, to derive the relationship between signals,  
 214 concentrations and  $f_{mud}$ . It is worth noting that the Curve Fitting Tool allows different func-  
 215 tions, for consistency across all combination of sensors, we decided to choose the functions  
 216 that provide highest  $R^2$  rather than predefine a function form for a certain relationship.

217 Figure 2a shows the relationships between raw signals of  $O_{700}$  and  $A_8$  from C1. As can be  
 218 seen, each line in Figure 2a is associated with a certain slope or  $f_{mud}$ , indicating that the ratio  
 219 of raw signals of  $O_{700}/A_8$  is independent of concentration and only depends on the fraction  
 220 of mud/sand in suspension. Subsequently, Figure 2b was produced by plotting  $f_{mud}$  against  
 221  $O_{700}/A_8$  ratios to obtain Eq. 1. Eq. 1 demonstrates that the fraction of mud/sand in a suspension  
 222 can be estimated from raw signals of  $O_{700}$  and  $A_8$ . Figure 2c,d shows the results when applying  
 223 a similar procedure to  $A_8$  signals and concentrations. A linear relationship between  $A_8$  signals  
 224 and concentrations is also seen. Eq. 2 is then achieved based on the relationship between  
 225 ratio of Concentration/ $A_8$  signals and  $f_{mud}$ . The same mechanism is applied to suspended  
 226 concentrations and  $O_{700}$  signals (Fig. 2e,f), to get Eq. 3.

$$f_{mud} = 49 \log_{10}(O_{700}/A_8) + 127 \quad (R^2 = 0.91) \quad (1)$$

$$(Concentration/A_8) = 0.014 f_{mud}^{1.13} + 1.95 \quad (R^2 = 0.80) \quad (2)$$

$$(Concentration/O_{700}) = 25 e^{-0.01 f_{mud}} \quad (R^2 = 0.90) \quad (3)$$

227 Equations 1, 2, and 3, offer two ways to calculate total concentration. Starting with one  
228 pair of raw optical/acoustic signals:

229 • **Step 1:** obtain  $f_{mud}$  via Eq. 1.

230 • **Step 2:**  $f_{mud}$  then can be substituted to

231 Eq. 2 to obtain  $Ca = A_8 * (0.014f_{mud}^{1.13} + 1.95)$  (2a)

232 Eq. 3 to obtain  $Co = O_{700} * (25e^{-0.01f_{mud}})$  (2b)

233 In this manuscript, Ca and Co refer to the estimated concentrations using acoustic (Eqs.  
234 1 & 2) and optical (Eqs. 1 & 3) signals, respectively. For example, SCI-C12-Co refers to the  
235 SCI functions (Eqs 1,2,3) which were derived from the data set C12 and were used to estimate  
236  $f_{mud}$  and concentration via **Step 1** and **2b**. It is noted that equations 1, 2, and 3 should be  
237 mathematically related. An example of a mathematical form of SCI functions is given in the  
238 Appendix A.

### 239 **3.2 Application: single pair ( $O_{700}$ , $A_8$ )**

240 This section further examines the reliability and accuracy of the SCI functions. Predicted  $f_{mud}$   
241 and total concentrations were acquired by applying equations 1, 2, and 3 to C1 data (Fig. 3).  
242 Overall, the functions underestimate  $f_{mud}$ , and concentration by 10% (Fig. 3a,b,c). There are  
243 two potential explanations for these underestimates. First, for pure mud and pure sand con-  
244 ditions, the differences between optical and acoustic signals are at their largest magnitudes.  
245 This is because in pure mud conditions, the optical signal is at its highest value, whereas the  
246 acoustic signal is at its lowest value. The opposite trend is seen in pure sand conditions, where  
247 the acoustic sensor is much more sensitive to changes in concentrations of sand than the opti-  
248 cal sensor. Hence, the errors in predictions of  $f_{mud}$  in these two particular cases are relatively  
249 high, especially with extremely low or extremely high concentrations, leading to accumulated  
250 errors throughout the calculation process (Fig. 3d,h). Second, the mathematical forms, e.g.,  
251 log (Eq. 1), power (Eq. 2), exponential (Eq. 3), or linear are an important factor that impacts

252 the performance of the method. Conducting a thorough sensitivity analysis of each different  
253 mathematical form on the overall accuracy of the SCI method is out of the scope of this paper.  
254 For simplicity and consistency, we decided to choose the function that provides the highest  $R^2$ .  
255 Readers are referred to (Pearson et al., 2021) for additional information of how different func-  
256 tions, especially hyperbolic tangent function, dictate the performance of the method. Figure 3  
257 also shows that the Co (Step 2b) approach provided slightly better results compared to Ca (Step  
258 2a) approach. Specifically, Figure 3c reveals that the histogram of estimated concentrations in  
259 percentages of Co is sharper with a smaller standard deviation than that of Ca. Figure 3e,f,g also  
260 reveals these differences between the two ways of calculation, albeit the differences seem to be  
261 insignificant for this pair of  $O_{700}$  and  $A_8$ .

### 262 **3.3 Application: All pairs**

263 In the previous section, the pair ( $O_{700}$ ,  $A_8$ ) was used as an example to explicate the procedure  
264 of 1) derivation and calibration of SCI functions, 2) calculation of  $f_{mud}$ , and 3) calculation of  
265 total concentrations, Ca and Co. In this section, the same procedure is applied for other pairs of  
266 optical/acoustic signals as well as experimental data C12 (all combinations are in the Appendix  
267 B).

268 Figure 4 summarizes the results of four pairs, ( $O_{852}$  -  $A_6$ ), ( $O_{420}$  -  $A_6$ ), ( $O_{852}$  -  $A_4$ ), and ( $O_{420}$ ,  
269  $A_4$ ). Overall, Figure 4 shows similar patterns between signal- $f_{mud}$  and signal-concentration  
270 as seen in Figure 2b,d,f which is different  $f_{mud}$  is associated with one unique ratio of opti-  
271 cal/acoustic signal. Unlike Figure 2, Figure 4 used data from both C1 and C2 experiments.  
272 Hence, the SCI functions were derived based on the combined behaviors of S1 and S2. It is  
273 also reminded that all the sensors are working concurrently, measuring the same suspension at  
274 very similar elevation in the water column. As such, Figure 4 provides important information  
275 regarding the behavior of optical/acoustic sensors to different SPM compositions. First, for the  
276 same type of acoustic device, the SCI functions are in similar forms (Fig. 4a,b); yet, with dif-  
277 ferent coefficients depending on the SPM compositions, the wavelengths and frequencies, as

278 well as the working mechanisms of the sensors. For example, a closer examination of Figure  
279 4a,b,e shows that the SCI functions are influenced by different wavelengths and frequencies to  
280 a greater degree than they are by particle sizes. That means that without prior knowledge of the  
281 suspension, i.e., particle sizes, it is possible to use a single SCI function to estimate  $f_{mud}$  and to-  
282 tal concentration. Second, Figure 4a,b illustrate that moving from longer to shorter wavelengths  
283 will shift the SCI functions to the right or down. Third, due to the differences in principles of  
284 operation, the SCI functions are also different, e.g, between  $A_6$  and  $A_4$  in comparison to  $O_{852}$   
285 and  $O_{420}$ . For example, Section 2.2.1 points out that the relationships between optical- $A_6$  is  
286 a log-linear and between optical- $A_4$  is a power function. This is one of the main issues when  
287 applying the SCI functions to wider range of different sensors.

288 Figures 5 and 6 further examine the results from  $C_{set}$ . Figure 5 presents the differences  
289 in percentage between true and estimated concentrations, i.e., between  $C_{measured}$  and  $C_a$ ,  $C_o$ ,  
290 obtained by SCI functions derived from C12 data. Figure 5 shows that majority of the error in  
291 predicting concentration falls within the range of  $\approx 50\%$ . Figure 5 also reveals that  $C_o$  method  
292 across all pairs is more consistent and accurate than that of  $C_a$ . In other words, there is no  
293 remarkable difference between different optical sensors, and thus wavelengths are not a critical  
294 parameter in our case. In contrast, the choice of acoustic frequencies dictates the accuracy  
295 substantially, e.g., at 1, 2  $MHz$  (Fig. 5g, i). This is also the reason why Optical- $A_{0.5}$  pairs were  
296 not included in Figure 5: they over/under-estimated  $f_{mud}$  and concentration in several orders  
297 of magnitudes. According to Rayleigh regime, this is expected because lower frequencies are not  
298 sensitive to the sands used in the experiments ( $d_{50}= 110$  and  $240 \mu m$ ). This observation will be  
299 discussed further in Section 5. Another observation from Figure 5 is that among all wavelengths,  
300 the wavelength of  $700 nm$  often produces larger errors (Fig. 5b, the red line). This is because  
301 of poor resolution of the  $O_{700}$ , particularly at low concentration in S2 dominating conditions,  
302 essentially provides the same output signals ( $< 1 NTU$ ) despite the increase in concentration  
303 from  $25$  to  $100 mg/L$ .

304 Figure 6 compares the performance of 1) different SCI functions derived from C12 but

305 apply for C1, C2, and C12 data sets, separately and 2) each optical/acoustic pair in terms of  
306 bias and root mean square error (RMSE). Figure 6 confirms the observations from Figure 5 that  
307 are the Co method provides better estimation of  $f_{mud}$  and concentration than Ca method. In  
308 addition, an RMSE of 10  $mg/L$  over a range of concentration from 15 to 200  $mg/L$  is a rela-  
309 tively good prediction of concentration, especially when the knowledge of the suspension is  
310 unknown. The influence of frequencies on the Ca method is revealed via different clusters of  
311 shapes, which represent different acoustic sensors (Fig. 6a,c,e).

#### 312 4 VALIDATION

313 Unlike  $C_{set}$ , in  $V_{set}$  we conducted experiments with mixtures of Bentonite, S1, and S2 at dif-  
314 ferent fractions (Table 2). The  $V_{set}$  allows us to verify 1) the size-dependency of SCI functions  
315 and 2) whether the SCI functions, derived from  $C_{set}$ , are applicable to a broader range of con-  
316 ditions. There are two notes associated with Figure 7. First, results from  $C_{set}$  shows that the  
317 pairs optical-A<sub>2</sub> provide much less accurate estimations. Hence, optical-A<sub>2</sub> pairs were excluded  
318 in this analysis. Second,  $V_{set}$  conditions 4 and 5 in Table 2 (or Figures 7d,e), are quite similar  
319 due to the uncertainties in controlling the amount of S2 which was partially deposited during  
320 the experiments. Nevertheless,  $V_{set}$  successfully creates distinctive SPM concentrations with  
321 different ratios of Bentonite, S1, and S2.

322 Figure 7 highlights two groups of the same data population: 1) all optical/acoustic pairs,  
323 i.e., the small inset figures and 2) the extractions (zoom in) of the most accurate estimation  
324 within  $\pm 10\%$  for both  $f_{mud}$  and concentration. In general, SCI-optical functions (filled mark-  
325 ers) present in all conditions, confirming that this method is accurate and practical. Another  
326 observation is that whether or not SCI functions can reasonably predict  $f_{mud}$  depends heavily  
327 on the percentage of Bentonite in the mixture. For example, an increase in the absolute amount  
328 of coarser sediment leads to decrease in the accuracy of  $f_{mud}$  calculation (Fig. 7a' - f'). In mud-  
329 dominated environment (Fig. 7a,b,f), SCI-C12 and SCI-C1 functions offer adequate estima-  
330 tions. When the mixture becomes coarser, S2 dominant, as in Figure 7c, the best SCI functions

331 change to SCI-C2-acoustic, i.e., more open markers presented. This is because acoustic sen-  
332 sors capture the changes in sand sizes better than optical sensors do, particularly for sand S2.  
333 Similarly, in S1 dominant conditions, Figure 7d,e, SCI-C1 functions have the best performances.

## 334 5 DISCUSSION

### 335 5.1 Frequency/wavelength and particle size

336 This section discusses the possibility of applying our proposed method to field measurements  
337 where the contents of the SPM are often unknown, e.g., mud/sand fraction in estuaries.  $V_{set}$   
338 is a test of schematic mixtures that might be observed in field measurements, offering a much  
339 more complicated environment compared with  $C_{set}$  from which the SCI-C12 functions were  
340 derived.  $V_{set}$  provides double the range of concentrations and different ratios of Be, S1, and  
341 S2 in comparison to  $C_{set}$ . Figure 8 shows the RMSE, indicating how well, the SCI-C12 functions  
342 work under bimodal (C1 and C2) and multimodal ( $V_{set}$ ) particle size distribution environments.  
343 Visually, higher acoustic frequencies ( $>4 MHz$ ) often result in better estimation compared to  
344 lower acoustic frequencies (1 and 2  $MHz$ ). Regarding  $V_{set}$ , SCI-C12 functions correctly repro-  
345 duce the mud/sand fraction from 8 to 26% of uncertainty with frequencies from 2 to 6  $MHz$   
346 (Fig. 8c).

347 The applications of SCI-C12-acoustic (Fig. 8d,e,f), however, generate erroneous outcomes  
348 ( $> 100\%$ ) except for optical- $A_6$  pair (Fig. 8f). There are a few notes concerning the performance  
349 of the SCI-C12 functions. It is clear that the accuracy declines with the increase of complex-  
350 ity of the mixtures, i.e., from  $C_{set}$  to  $V_{set}$ . Additionally, instead of 30 data points as in C1 and  
351 C2, there are only 6 data points in  $V_{set}$  (Table 2). Hence, the weight of one error is exaggerated  
352 and somewhat skews the RMSE calculation. The low resolution of sensor  $O_{700}$  and  $A_8$  at lower  
353 concentrations also plays an important role in reducing the performance of the SCI-functions.

354 The finding that optical- $A_6$  pair is one of the best combinations becomes clear when put  
355 in the context of scattering theory, i.e.,  $2\pi r\lambda^{-1} \approx 1$ . The optimal particle diameters for acous-  
356 tic at frequencies 4 and 6  $MHz$  are 120 and 80  $\mu m$ , respectively. If we calculate a hypothetical

357 mean particle diameter for each condition in  $V_{set}$  as  $d_{avg} = \sum_i^n d_i p_i$  where  $d_i$  is the particle size  
358 of size fraction  $i$  (Bentonite = 40, S1 = 110, S2 = 240  $\mu m$ ), and  $p_i$  is the percentage by mass of size  
359 fraction  $i$  (Table 2). The results show that the values of  $d_{avg}$  vary from 40 to 136  $\mu m$  which is  
360 just around the optimal working ranges of frequencies 4-6  $MHz$ . This might explain why SCI-  
361 optical-A<sub>4,6</sub> functions almost always produce the most accurate predictions in both  $C_{set}$  and  
362  $V_{set}$ . Application of the same theory helps to explain why lower frequencies,  $< 2 MHz$ , some-  
363 times generate errors in prediction by several order of magnitude, because those frequencies  
364 are only sensitive to much larger particle sizes. The miscalculation of SCI-optical-A<sub>8</sub> pairs for  
365  $V_{set}$ , however, is not easy to explain since the sensor A<sub>8</sub> only provides final output in the form  
366 of mass concentration without revealing the inversion function used or the raw signal. The  
367 differences between  $C_{estimated}$  and  $C_{measured}$  escalate with the increase of sand size, concen-  
368 tration and complexity degree, i.e., multimodal size distribution, of the suspension. Therefore,  
369 one possible conclusion from Figure 7 and 8 is that A<sub>8</sub> sensor does not work properly under  
370 multimodal and/or coarser sand particle environments.

371 In a relatively different pattern, optical sensors are quite consistent and offer much lower  
372 variations in  $f_{mud}$  and total concentration predictions. Further investigation of coefficient  
373 of variations (standard deviation/mean) shows that optical sensors are more sensitive to the  
374 change of  $f_{mud}$ , while acoustic sensors are more sensitive to the change of particle sizes. For  
375 example, a reduction in  $f_{mud}$  from 100 to 0% results in an increase in O<sub>700</sub> signal of 6.1%, but  
376 only 0.6% for A<sub>6</sub> signal. In contrast, signal differences between S1 and S2 conditions for O<sub>700</sub> is  
377 almost 4.1%, while for A<sub>6</sub> is  $\approx 10\%$ . Thus, the homogeneity or complexity of the mixture are not  
378 as important for optical sensors as for acoustic sensors.

## 379 5.2 Multi-frequency or multi-wavelength

380 A question of interest is whether the same procedure is applicable to two paired optical sen-  
381 sors or two paired acoustic sensors of different wavelengths/frequencies. Inversion of multi-  
382 frequency acoustic backscatter data to obtain sediment size and concentration profile often re-

383 quires some prior knowledge of the suspension and a suitable computational algorithm (Moate  
384 and Thorne, 2009; Lynch et al., 1994; Thorne and Hurther, 2014; Thorne et al., 2021). The  
385 present study does not intend to make comparison between our approach and other existing  
386 methods. Rather, we would like to discuss a possible way to take advantage of multi-wavelength  
387 and/or multi-frequency measurements to achieve similar results. Figure 9 highlights a few ex-  
388 amples of combinations of different wavelengths/frequencies. While no useful information  
389 could be extracted from optical-optical pairs (Fig. 9), the relationship between multi-frequency  
390 measurements is very promising, alike Figure 4c,d. For example, in Figure 9a-c, pure Bentonite  
391 and pure sand conditions are still set a clear boundaries for all other intermediate ratios of  
392 mud/sand. A certain slope/intercept associated with each condition also holds for a specific  
393 mud/sand ratio. Differences between finer and coarser sand particle sizes are seen in some  
394 cases (Fig. 9a,b,c). Nevertheless, providing a full calculation for SCI-acoustic-acoustic func-  
395 tions is out of the scope of this study. In future, this approach will be further investigated.

## 396 6 CONCLUSIONS

397 This study proposes a new approach to obtain mud/sand fraction and the total concentration  
398 of a suspension based on conjugating optical-acoustic measurements. Two sets of experiments,  
399 providing bimodal ( $C_{set}$ ) and multimodal ( $V_{set}$ ) particle size distributions, are used to calibrate  
400 and validate our SCI functions. In general, SCI-optical functions have a better performance  
401 than their counterpart SCI-acoustic functions. The results show that for suspension in which  
402 the particle size is known (e.g., SCI functions were chosen accordingly) predicted concentra-  
403 tions can be as accurate as  $\approx 7 \text{ mg/L}$  (Fig. 6). Without prior knowledge of particle sizes, SCI  
404 functions derived from C12 can be applied to various sediment mixtures with a reasonable er-  
405 ror, i.e.,  $< 10\%$  for  $f_{mud}$  and  $< 15\%$  for concentration. For example, considering there is an  
406 average size for each condition in  $V_{set}$  the best optical-acoustic pairs are optical wavelength  
407 620-700  $nm$  and acoustic frequency 4-6  $MHz$ . The results suggest that the SCI method is highly  
408 applicable to sedimentary-dynamic environments, e.g., estuaries and coastal zones, even with-

409 out sensor calibrations and knowledge of mud/sand ratio. In the near future, the possibility of  
410 applying the same approach to multi-frequency acoustic measurements and a larger range of  
411 concentrations as well as different types of minerals and particle sizes will be investigated.

## 412 **7 ACKNOWLEDGEMENT**

413 This work was co-funded by Ifremer and the PHRESQUES project, coordinated by the GIP Seine  
414 Aval. PHRESQUES was funded by the CPIER «Vallée de Seine», the Seine Normandy Water  
415 Agency (AESN), and the Normandie and Ile de France Regions. This project is also supported  
416 by the eLTER «Zone Atelier Seine». We are also grateful for the critiques provided by Michael  
417 Fettweis during the preparation of this manuscript.

C [mg/L]	Bentonite/sand fraction ( $f_{mud}$ ) [%]			Task	Time [min]
	100	75, 50, 25	0		
15	(pure mud)	(mixed mud/sand)	(pure sand)	1. Bentonite stabilized in a beaker	0-30
25				2. Bentonite stabilized in DEXMES	30-60
50	C1_100	C1_75,50,25	C1_0	3. Introduce sand in DEXMES	55
100	or	or	or	4. Data recording	60-70
150	C2_100	C2_75,50,25	C2_0	5. Water sampling	71-73
200				6. New sediment for the next step	Repeat task 1-5

**Table 1:** Experimental conditions and procedure of the calibration set,  $C_{set}$ . S1: sand particle size  $d_{50} = 110 \mu m$ . S2: sand particle size  $d_{50} = 240 \mu m$ .

Run	C [mg/L]	Bentonite/sand fraction [%]			$d_{avg}$ [ $\mu m$ ]
		Be	S1 (110 $\mu m$ )	S2 (240 $\mu m$ )	
1	50 (46)	100 (100)	0 (0)	0 (0)	40
2	75 (68)	67 (67)	33 (33)	0 (0)	63
3	125 (103)	40 (44)	20 (21)	40 (35)	125
4	200 (174)	25 (26)	50 (54)	25 (20)	118
5	250 (191)	20 (23)	40 (45)	40 (32)	136
6	400 (330)	50 (54)	25 (31)	25 (15)	92

**Table 2:** Experimental conditions and procedure of the validation set,  $V_{set}$ .  $x$  (y): target (measured).  $d_{avg} = \sum_i^n d_i p_i$  where  $d_i$  is the particle size of size fraction  $i$ , and  $p_i$  is the percentage by mass of size fraction  $i$ .  $i$  denotes S1 and S2.

Sensor	Working frequency [MHz]	Sampling frequency	Data output	Notation in text	
	wavelength [nm]	[Hz]	unit		
Acoustic	LISST-ABS	8	1	mg/L	A <sub>8</sub>
	ADV Vector	6	32	SNR - dB	A <sub>6</sub>
	AQUAscat 1000R (Transducer 4 MHz)	4	32	count	A <sub>4</sub>
	AQUAscat 1000R (Transducer 2 MHz)	2	32	count	A <sub>2</sub>
	AQUAscat 1000R (Transducer 1 MHz)	1	32	count	A <sub>1</sub>
	AQUAscat 1000R (Transducer 0.5 MHz)	0.5	32	count	A <sub>0.5</sub>
Optical	HydroScat-4 (Channel 4)	852	1	m <sup>-1</sup>	O <sub>852</sub>
	Wetlabs_FLNTU	700	1	count -> NTU	O <sub>700</sub>
	HydroScat-4 (Channel 3)	620	1	m <sup>-1</sup>	O <sub>620</sub>
	HydroScat-4 (Channel 2)	532	1	m <sup>-1</sup>	O <sub>532</sub>
	HydroScat-4 (Channel 1)	420	1	m <sup>-1</sup>	O <sub>420</sub>

**Table 3:** A summary of working conditions of all sensors used in this study. Data from LISST-100X (not shown here) is used to verify the particle size distribution in suspension, but is not paired with other sensors during the data analysis process.

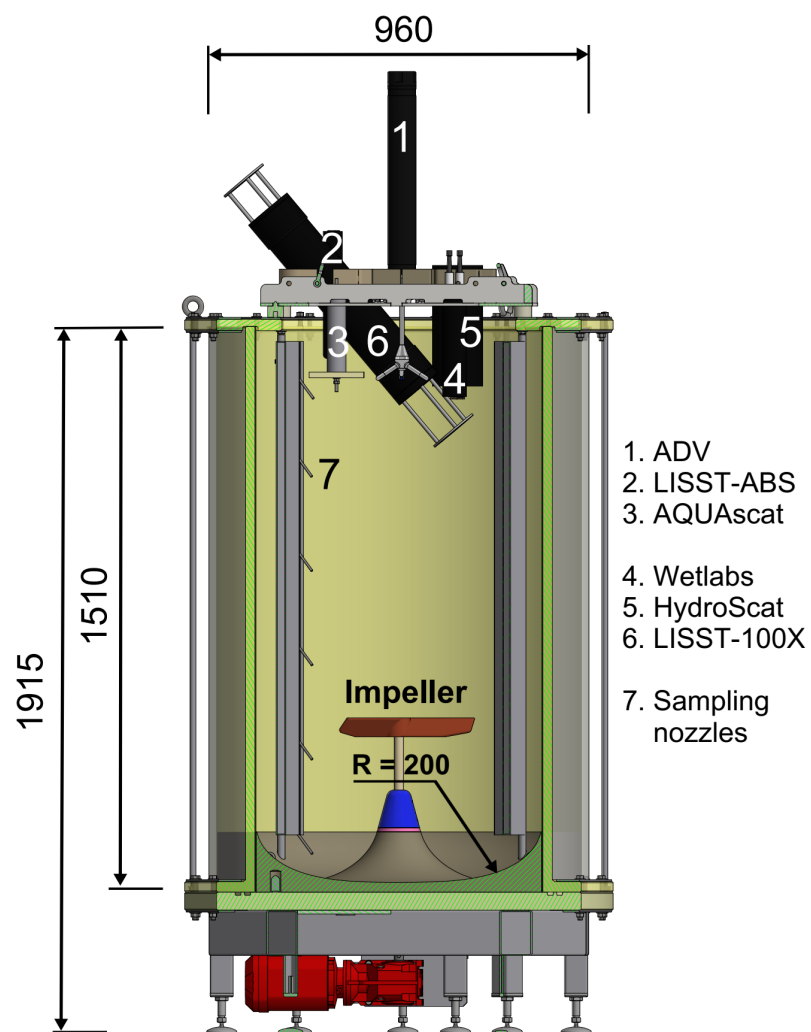


**Figure 1:** Experimental setup of the DEXMES tank (not to scale). Measuring volumes of all sensors were set at similar level as of water sampling nozzle,  $\approx 25$ - $26$  cm below the water surface.

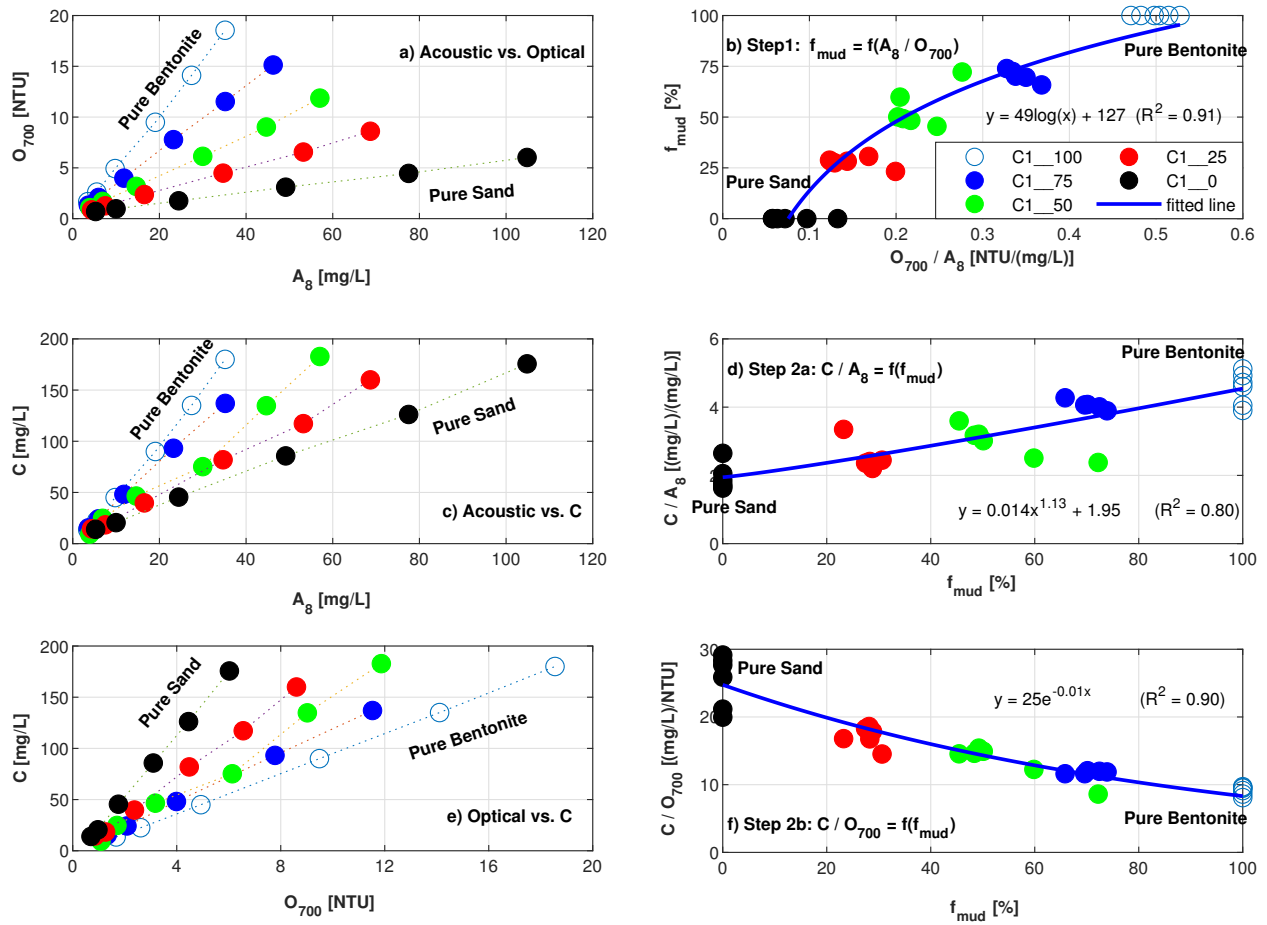


**Figure 2:** An example of relationships between  $O_{700}$  and  $A_8$  (Optical 700 nm and Acoustic 8 MHz) and total concentrations. Only Calibration set for sand S1 (C1) data were used in this demonstration. Step 1, 2a, 2b: please refer to equations 1, 2, and 3.

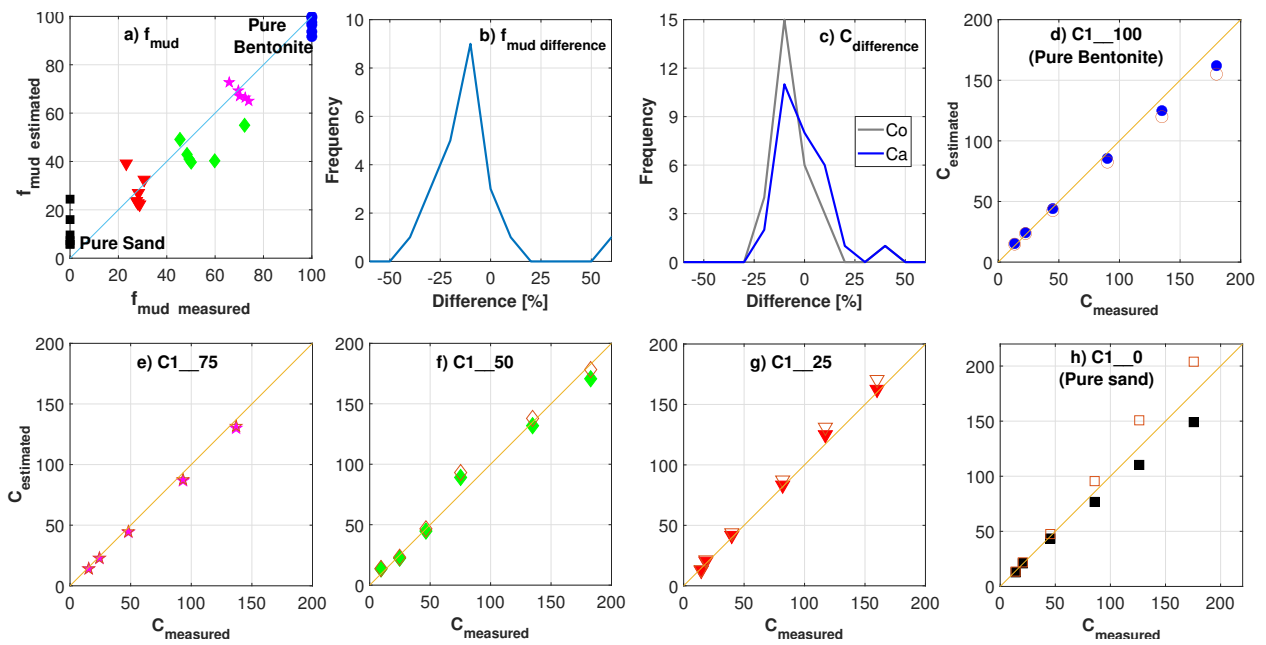


**Figure 3:** Differences between estimated and measured of  $f_{mud}$  and total concentration for the pair O<sub>700</sub>, A<sub>8</sub>. Ca: empty markers. Co: filled markers.

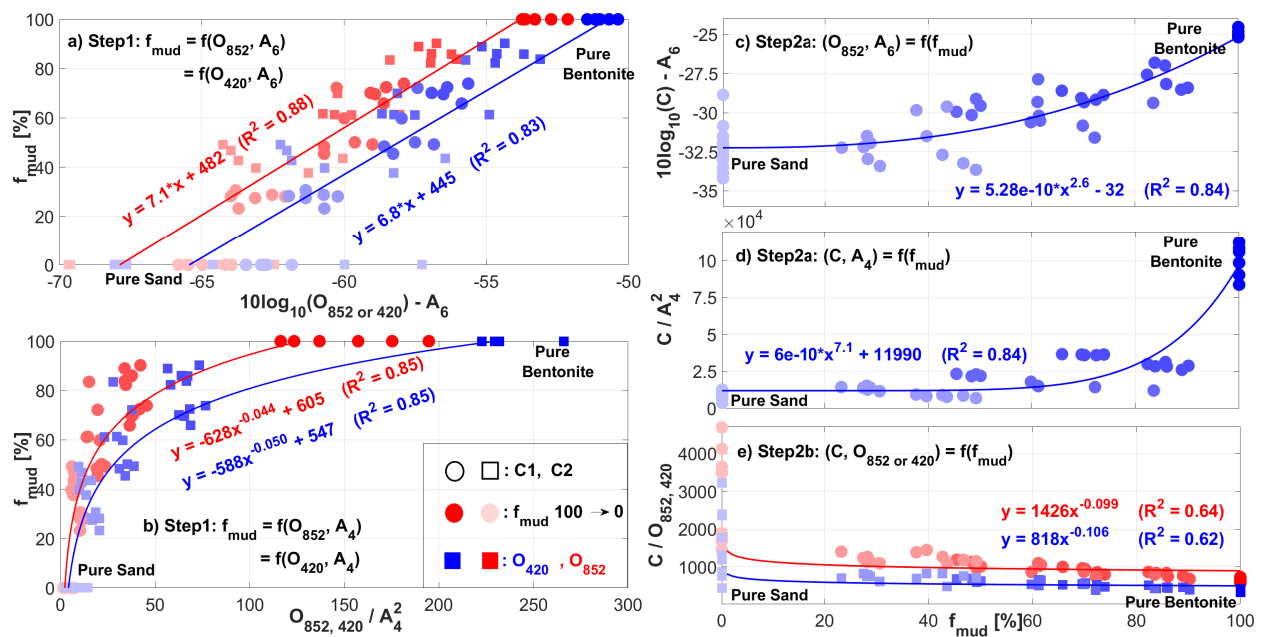


**Figure 4:** Application of SCI method to four optical/acoustic pairs with all data in *Cset* (C12). The reductions of  $f_{mud}$  from 100% to 0% are shown by the darkest color to lightest color. Blue: data from  $O_{420}$ . Red: data from  $O_{852}$ . The displayed functions are obtained from data set C12.

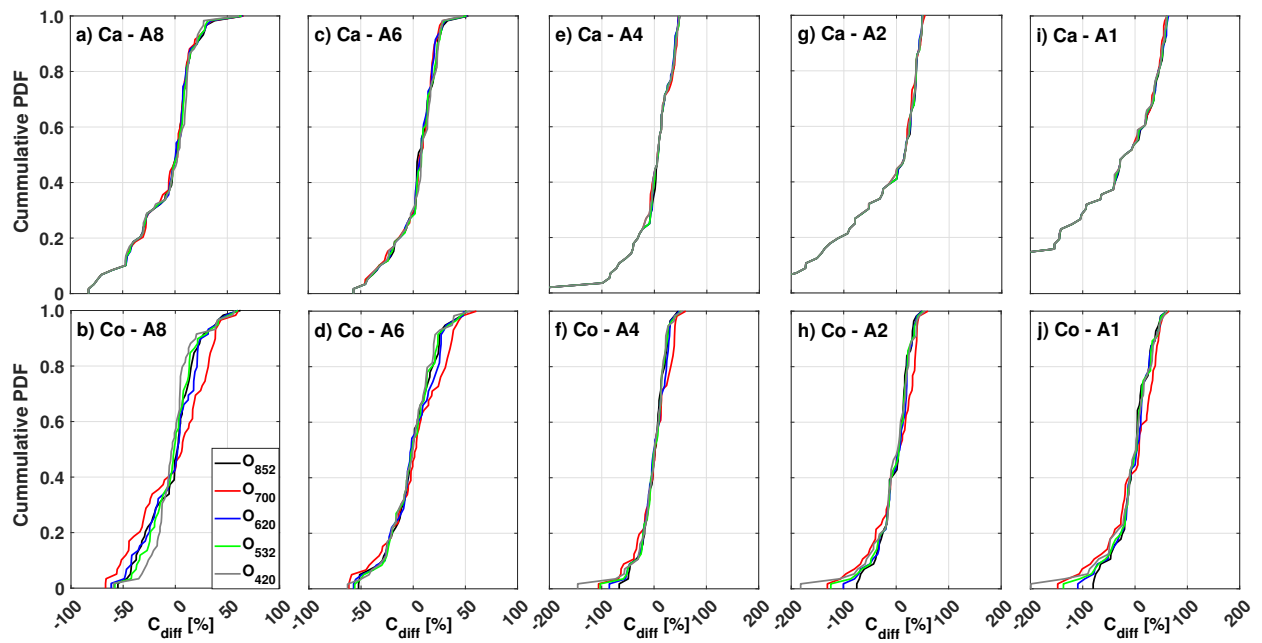


**Figure 5:** Comparison of all pairs when applying SCI-C12 functions to estimate Ca (step 2a) and Co (step 2b). Concentration differences, in %, between  $C_{measured}$  and Ca, Co.  $C_{diff} = \frac{(C_{measured} - C_{estimated})}{C_{measured}} 100\%$ .

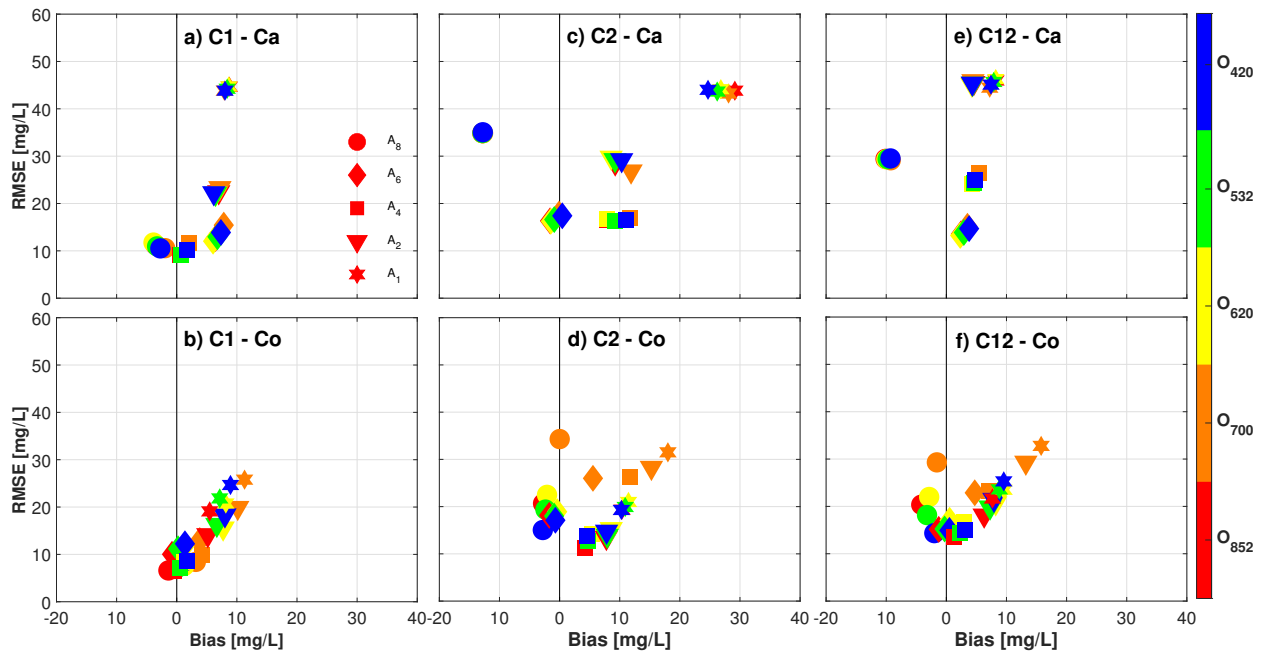


**Figure 6:** Comparison of the performances of different SCI functions obtained from different data sets, i.e., C1 (a, b), C2 (c, d) or C12 (e, f). RMSE and bias of each pair.  $Bias = \frac{\sum (C_{measured} - C_{estimated})}{m}$ .  $RMSE = \sqrt{\frac{\sum (C_{measured} - C_{estimated})^2}{m}}$ , where  $m$  is the number of data points.

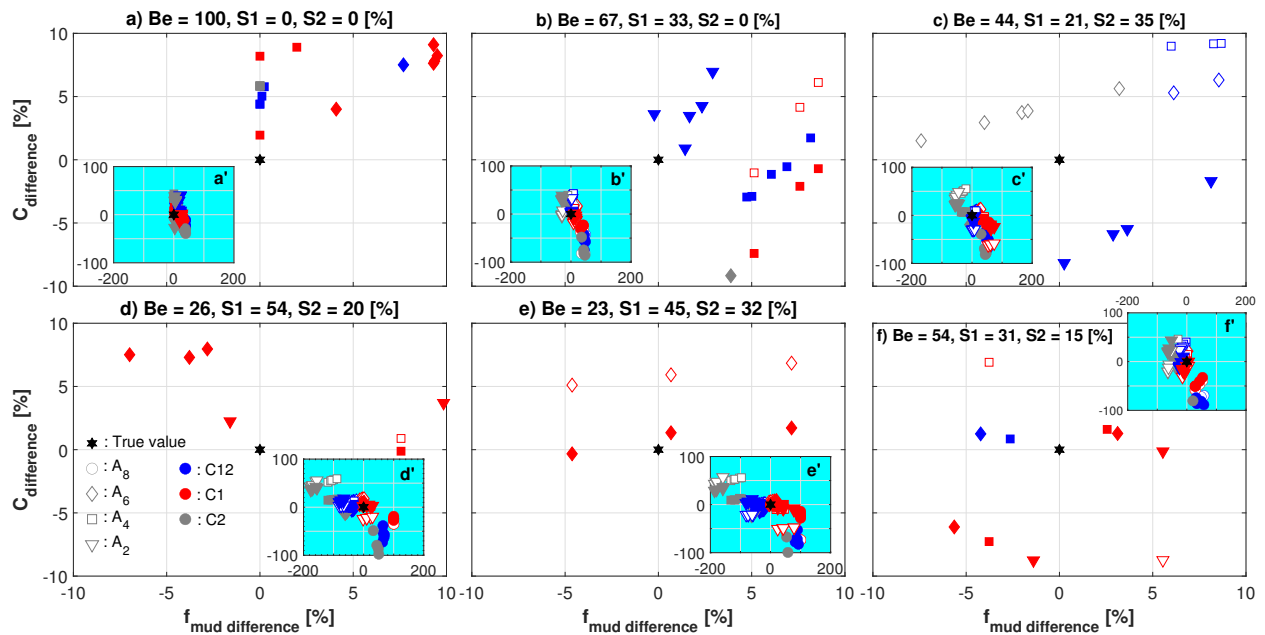


**Figure 7:** Application of SCI functions, derived from  $C_{set}$ , to  $V_{set}$  data. The sub-figures show all optical/acoustic pairs that predict  $f_{mud}$  and concentration within  $\pm 10\%$  error. The small inset inside each sub-figure shows results from all pairs of each experimental condition. The legend should be read as a combination of marker + color + filled/open. Where filled marker = Co, empty marker = Ca. For example, a blue-filled-diamond means Co was obtained by C12-( $O_{800} \rightarrow 420 - A_6$ ) functions.

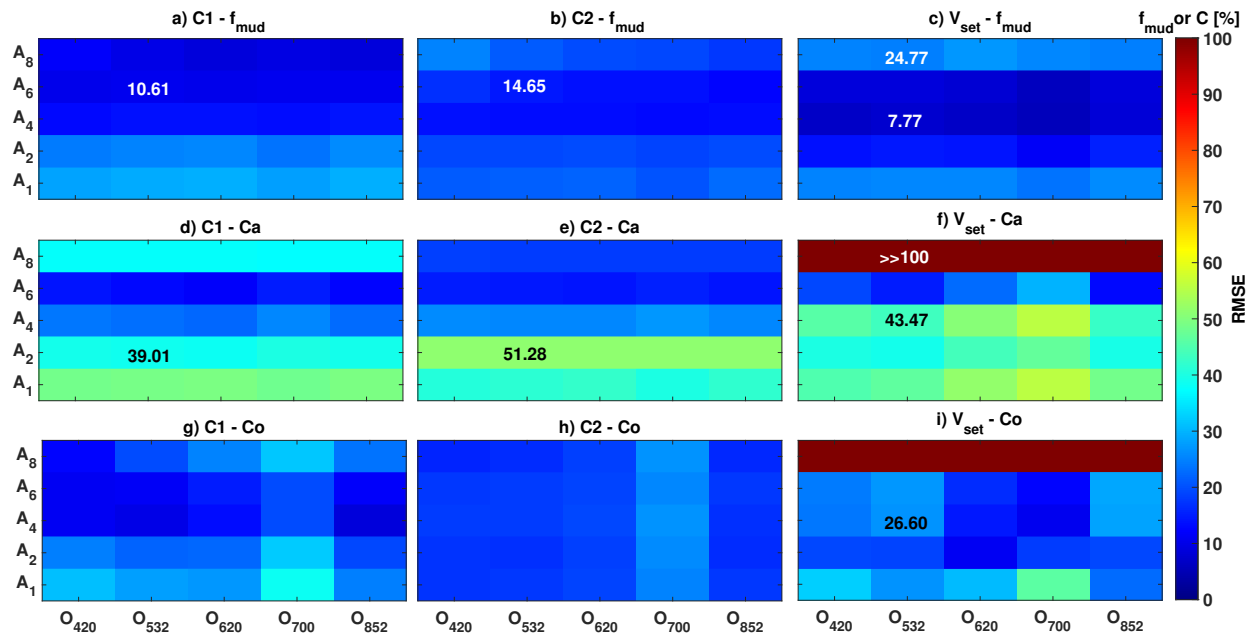


**Figure 8:** RMSE of the application of SCI-C12 functions to data sets C1, C2, and  $V_{set}$ .  $RMSE = \sqrt{(X_{measured} - X_{estimated})^2}$ , where  $X = f_{mud}$  or concentration. A few numbers associated with specific color are also given for better references. In this figure, SCI functions derived from data set C12 were applied to calculate Ca (step 2a) and Co (step 2b) of different data sets, i.e., from bimodal to multimodal particle size mixtures.

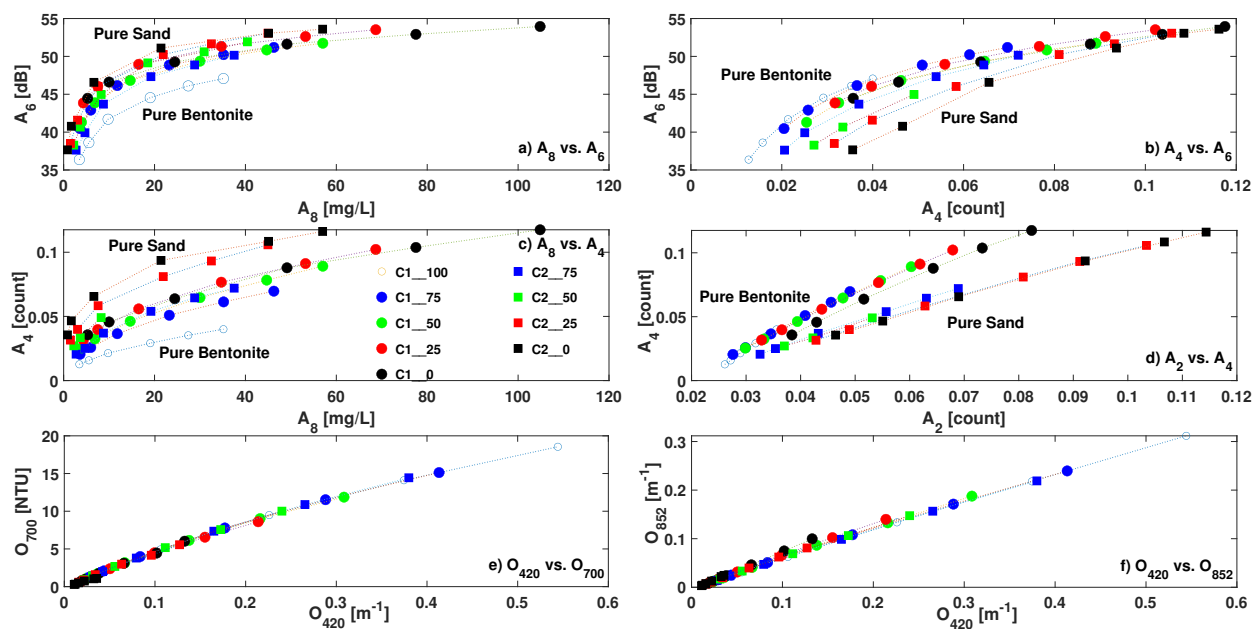


**Figure 9:** Examples of combinations of acoustic-acoustic, and optical-optical pairs. The two upper panels show similar pattern as seen in Figure 2, indicating that it is possible to derive a similar SCI functions from acoustic-acoustic data set, i.e., sub-figures a, b, c. All signals are raw, uncalibrated.

418 **A APPENDIX A. SCI FUNCTIONS - A FURTHER DISCUSSION**

419 In Section 3.1 we proposed to derive the SCI functions based on searching for the “optimal”  
420 functions, i.e., functions that have the highest  $R^2$ . Fundamentally, equations 2 and 3 should  
421 be able to combine into one equation in which optical and acoustic terms represent the mud  
422 and sand fractions, respectively. Figures 2a,c,e show that all conditions converge to point (0,0).  
423 Hence, the relationship between  $f_{mud}$  and ratio of  $O_{700}/A_8$  should have a linear form of  $y =$   
424  $a * x$ , as do the relationships between  $C$  and  $O_{700}$  and between  $C$  and  $A_8$ . The SCI functions –  
425 Equations 1, 2, and 3 – then can be written as:

$$f_{mud} = t * (O_{700}/A_8) \tag{A.1}$$

$$Concentration = m * f_{mud} * O_{700} + n * (100 - f_{mud}) * A_8 \tag{A.2}$$

426 where  $t$ ,  $m$ , and  $n$  are constants. Fitting data from Figure 2 to equations A.1 and A.2 gives  
427  $t = 200$ ,  $m = 0.1$  and  $n = 0.02$ . SCI functions written in the form of A.2 provide results that are  
428 very similar to equations 1 and 3. However, there are two primary drawbacks using equations  
429 A.1 and A.2. First, mud or sand reflects both optical and acoustic signals to different degrees.  
430 For example, the amount of sand needed to increase the optical signal by 10  $NTU$  might be  
431 several times the amount of mud. On the contrary, the amount of mud needed to increase the  
432 acoustic signal by 5  $dB$  might take several times the amount of sand. To date, the percentages  
433 of backscatter signals reflected by mud and by sand in a mixed suspension are not fully under-  
434 stood. Hence, mathematical expression of such behaviors is rather difficult, particularly in case  
435 of AQUAscat and ADV where the relationships are not linear. Second, the resolutions of the sen-  
436 sors used in these experiments are not high enough to differentiate between small increases in  
437 each concentration step and/or  $f_{mud}$ , e.g., from concentrations of 150  $mg/L$  to 200  $mg/L$ . Sub-  
438 sequently, derivations of coefficients such as  $t$ ,  $m$ , and  $n$  are not necessarily better than using  
439 empirical functions as shown in the main document.

## 440 **B APPENDIX B. SCI FUNCTIONS - ALL PAIRS**

441 This section provides the SCI functions of all the other pairs. In these figures, blue circles or red  
442 squares represent data from C1 or C2, respectively. Blue or red curves indicate the SCI functions  
443 obtained from either C1 or C2 data set. The mathematical functions displayed in the sub-figures  
444 were obtained from data set C12 (black line). As discussed in Section 3.2, for pure Bentonite and  
445 pure sand conditions only concentration  $C = 100$  mg/L was used to minimized the variations in  
446 these two extreme cases.

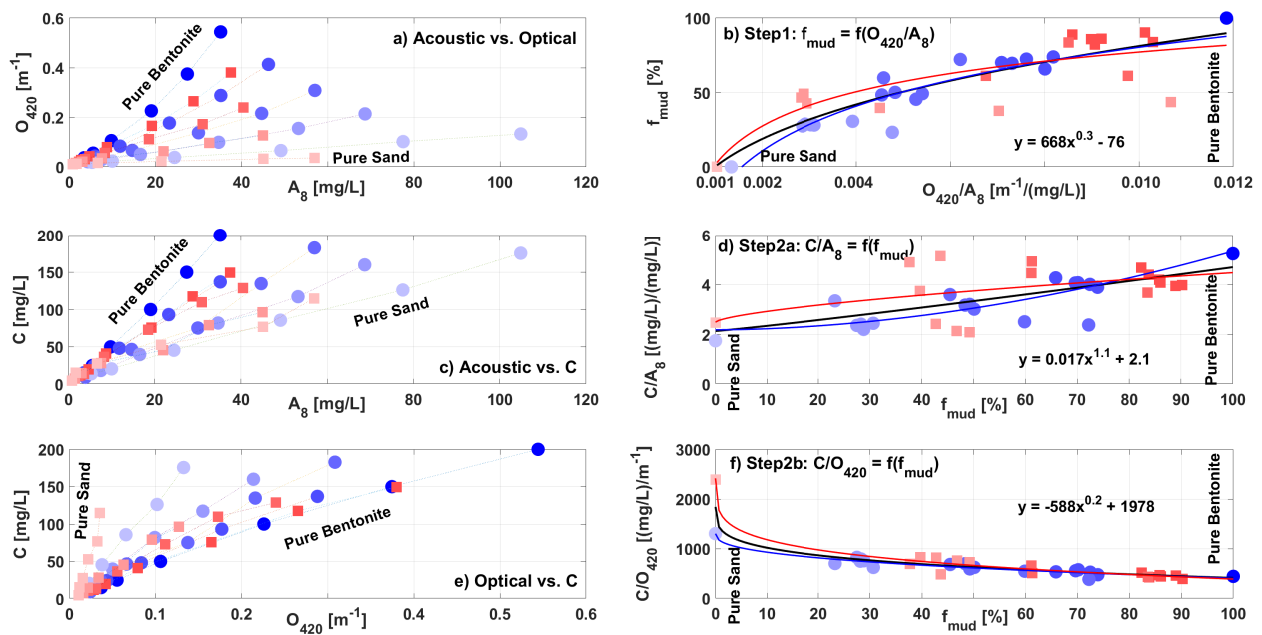


**Figure B1:** Application of SCI method to the optical/acoustic pair of  $O_{420}$  and  $A_8$  with data in C1 (blue), C2 (red) and C12 (black). The reductions of  $f_{mud}$  from 100% to 0% are shown by the darkest color to lightest color. The displayed function are obtained from data set C12.

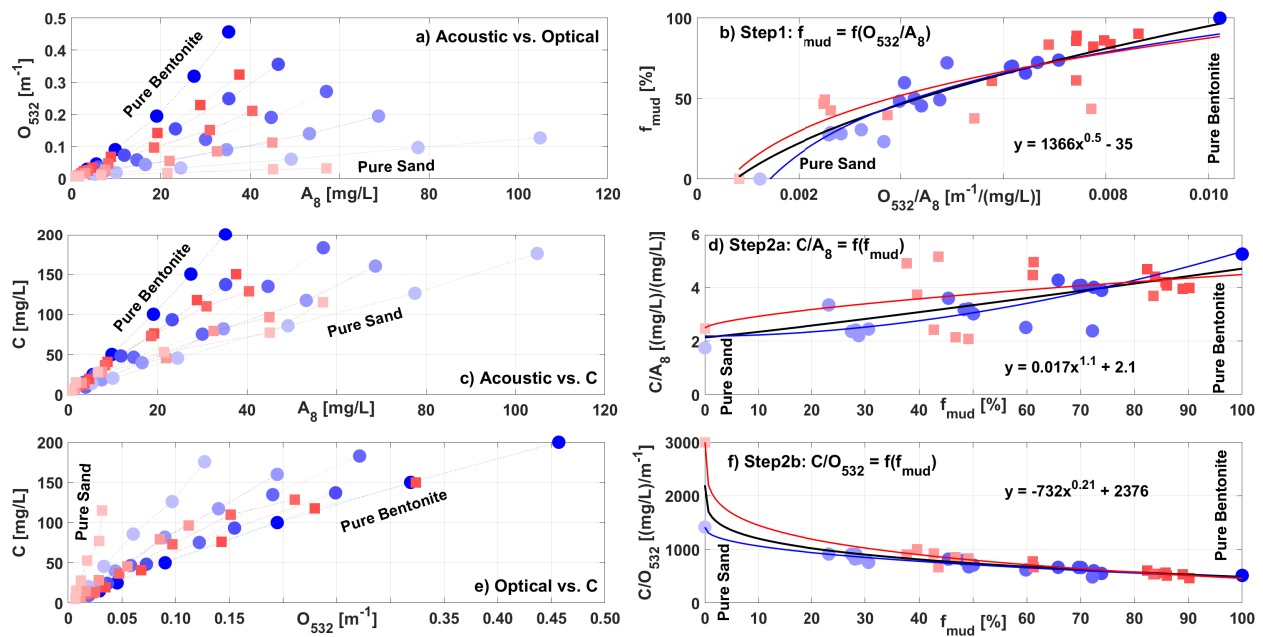


**Figure B2:** Application of SCI method to the optical/acoustic pair of  $O_{532}$  and  $A_8$  with data in C1 (blue), C2 (red) and C12 (black). The reductions of  $f_{mud}$  from 100% to 0% are shown by the darkest color to lightest color. The displayed function are obtained from data set C12.

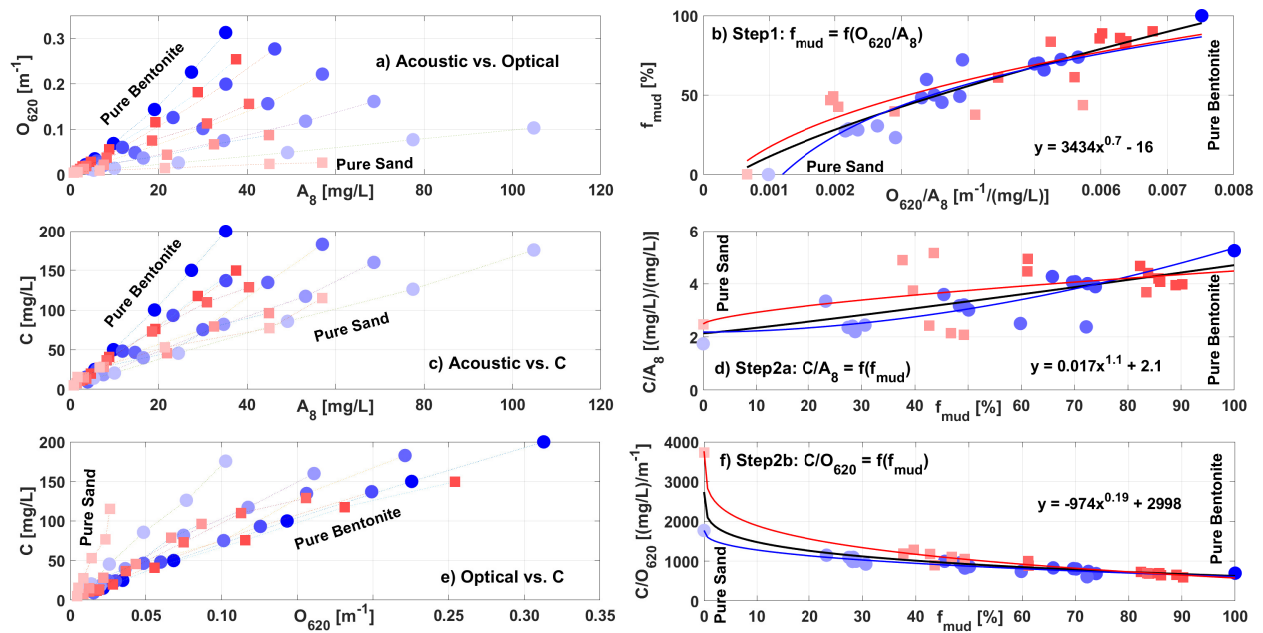


**Figure B3:** Application of SCI method to the optical/acoustic pair of  $O_{620}$  and  $A_8$  with data in C1 (blue), C2 (red) and C12 (black). The reductions of  $f_{mud}$  from 100% to 0% are shown by the darkest color to lightest color. The displayed function are obtained from data set C12.

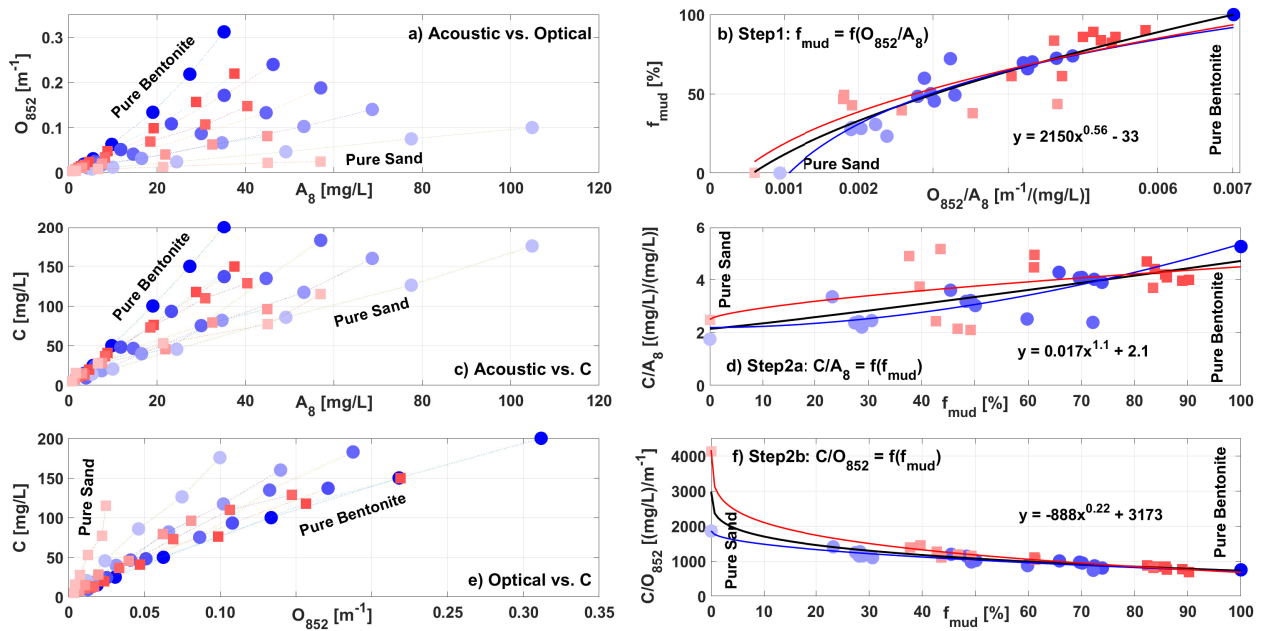


**Figure B4:** Application of SCI method to the optical/acoustic pair of  $O_{852}$  and  $A_8$  with data in C1 (blue), C2 (red) and C12 (black). The reductions of  $f_{mud}$  from 100% to 0% are shown by the darkest color to lightest color. The displayed function are obtained from data set C12.

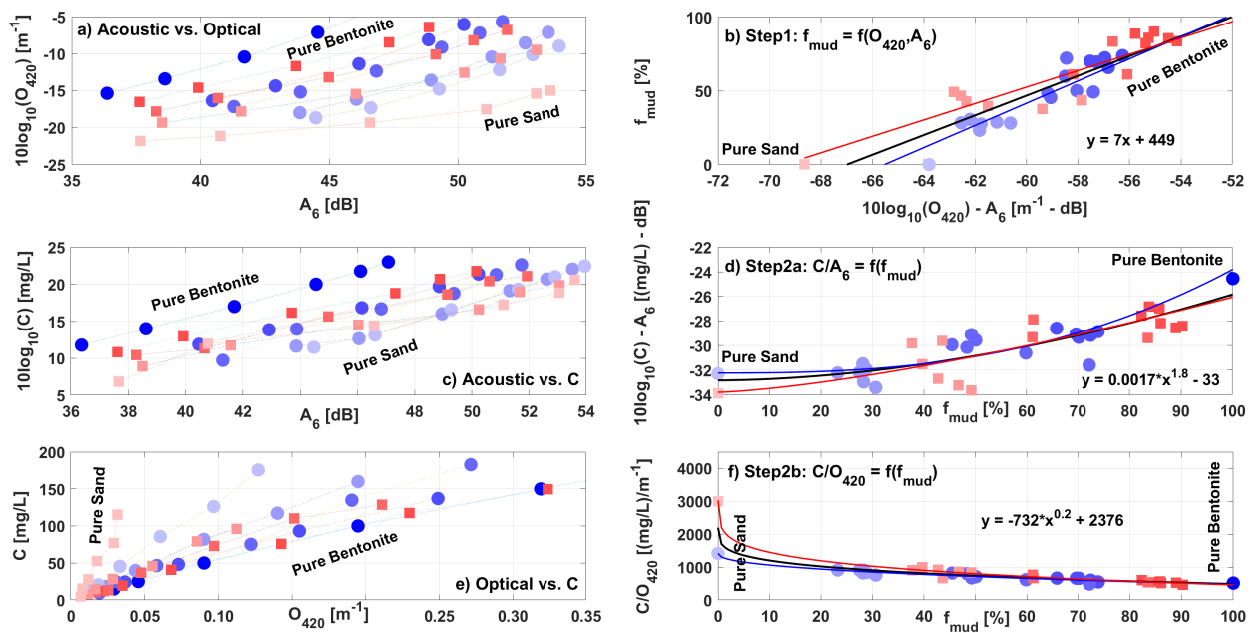


**Figure B5:** Application of SCI method to the optical/acoustic pair of  $O_{420}$  and  $A_6$  with data in C1 (blue), C2 (red) and C12 (black). The reductions of  $f_{mud}$  from 100% to 0% are shown by the darkest color to lightest color. The displayed function are obtained from data set C12.

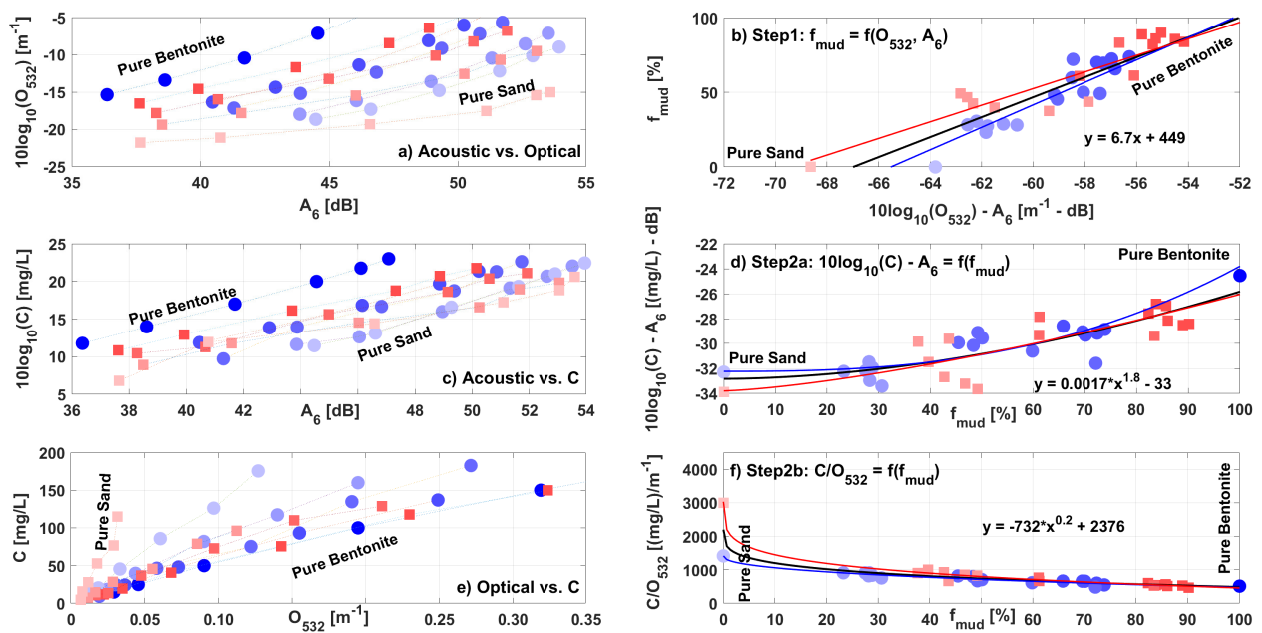


**Figure B6:** Application of SCI method to the optical/acoustic pair of  $O_{532}$  and  $A_6$  with data in C1 (blue), C2 (red) and C12 (black). The reductions of  $f_{mud}$  from 100% to 0% are shown by the darkest color to lightest color. The displayed function are obtained from data set C12.

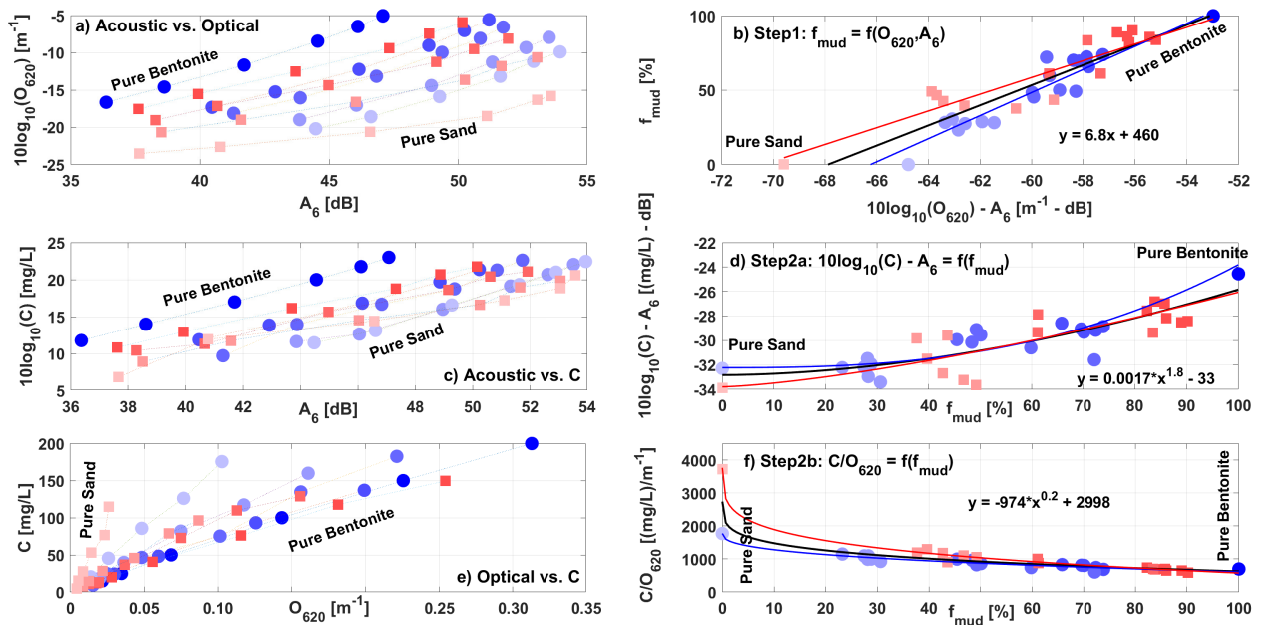


**Figure B7:** Application of SCI method to the optical/acoustic pair of  $O_{620}$  and  $A_6$  with data in C1 (blue), C2 (red) and C12 (black). The reductions of  $f_{mud}$  from 100% to 0% are shown by the darkest color to lightest color. The displayed function are obtained from data set C12.

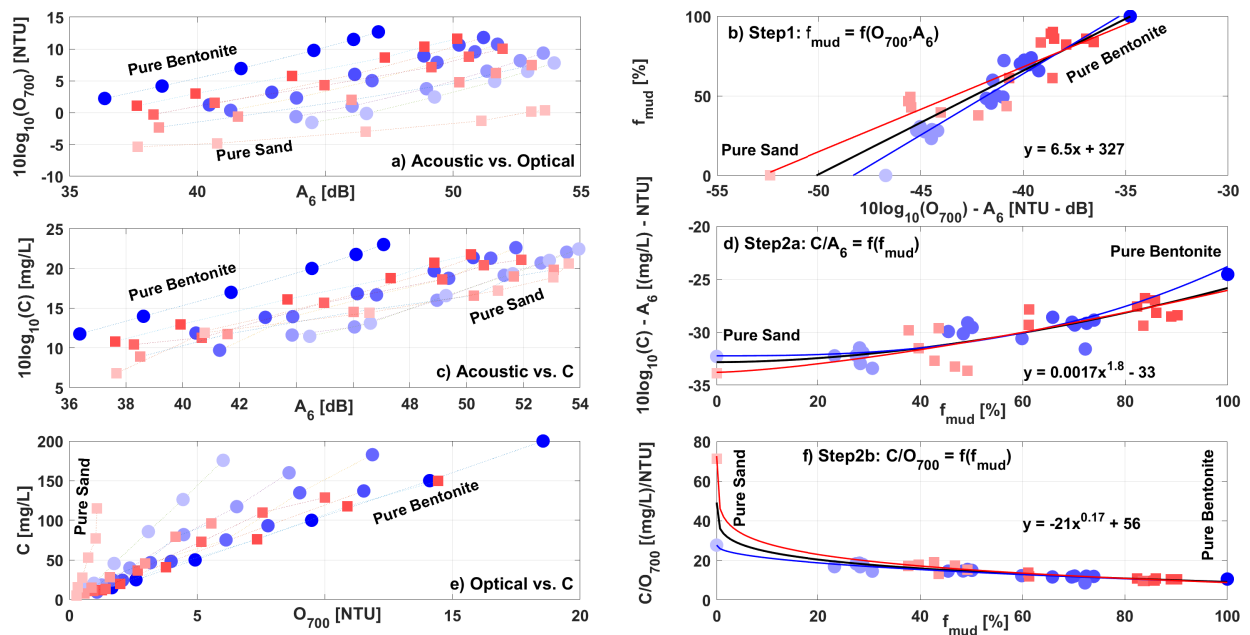


**Figure B8:** Application of SCI method to the optical/acoustic pair of  $O_{700}$  and  $A_6$  with data in C1 (blue), C2 (red) and C12 (black). The reductions of  $f_{mud}$  from 100% to 0% are shown by the darkest color to lightest color. The displayed function are obtained from data set C12.

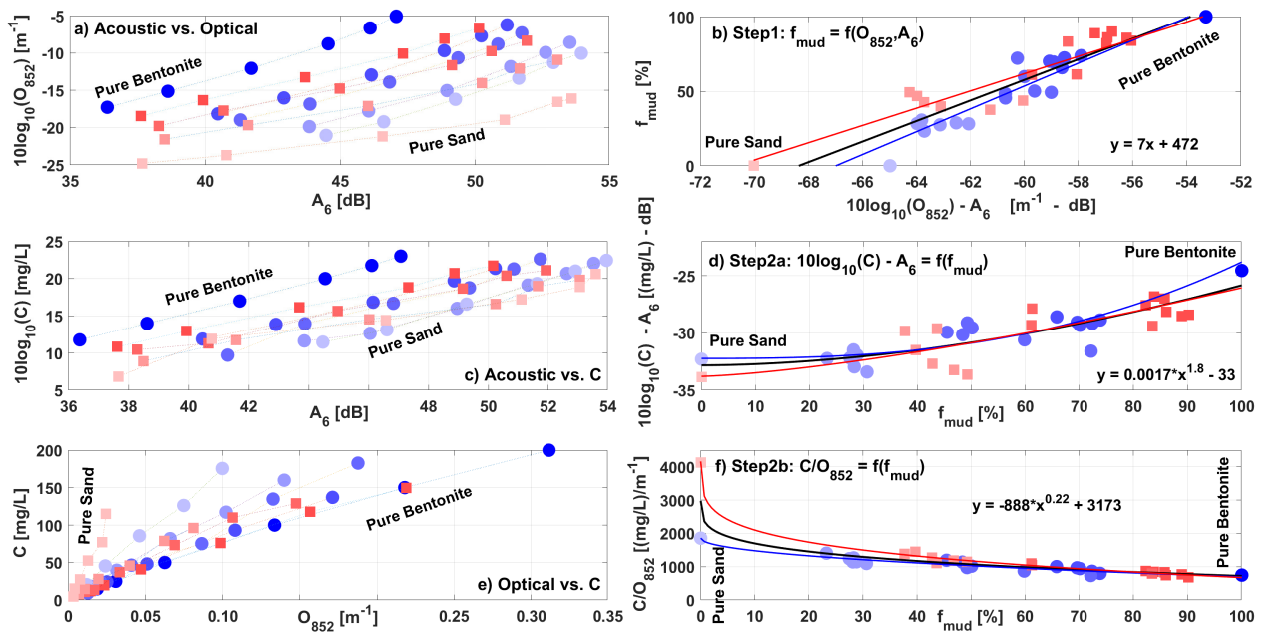


**Figure B9:** Application of SCI method to the optical/acoustic pair of  $O_{852}$  and  $A_6$  with data in C1 (blue), C2 (red) and C12 (black). The reductions of  $f_{mud}$  from 100% to 0% are shown by the darkest color to lightest color. The displayed function are obtained from data set C12.

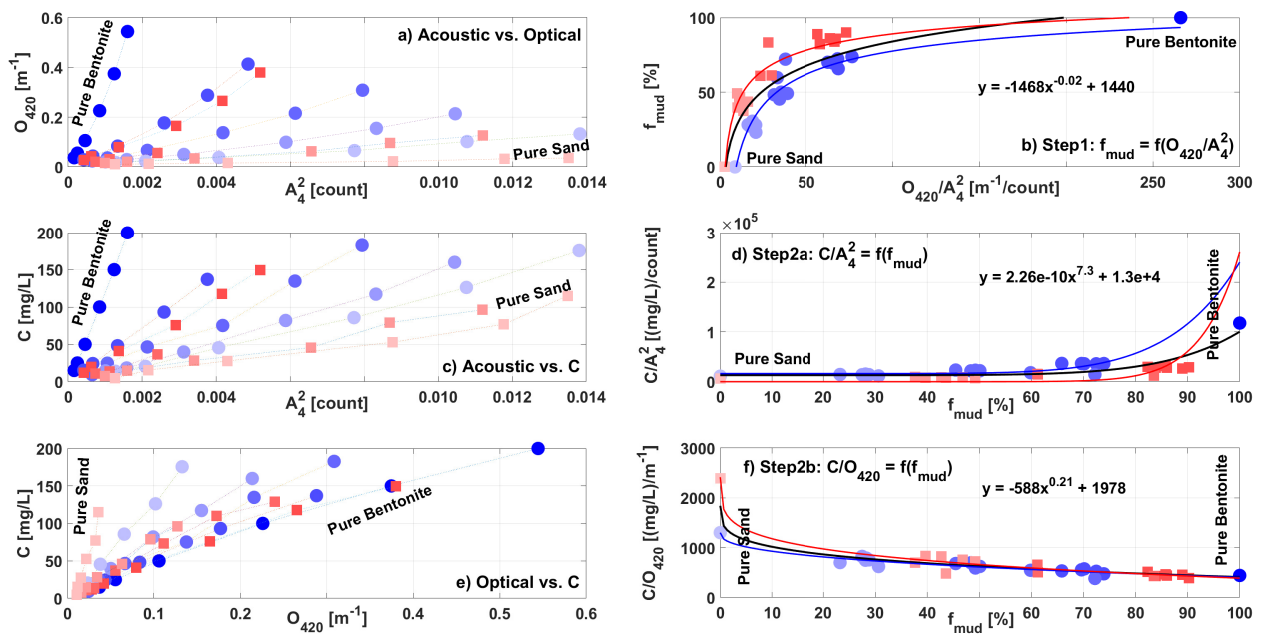


**Figure B10:** Application of SCI method to the optical/acoustic pair of  $O_{420}$  and  $A_4$  with data in C1 (blue), C2 (red) and C12 (black). The reductions of  $f_{mud}$  from 100% to 0% are shown by the darkest color to lightest color. The displayed function are obtained from data set C12.

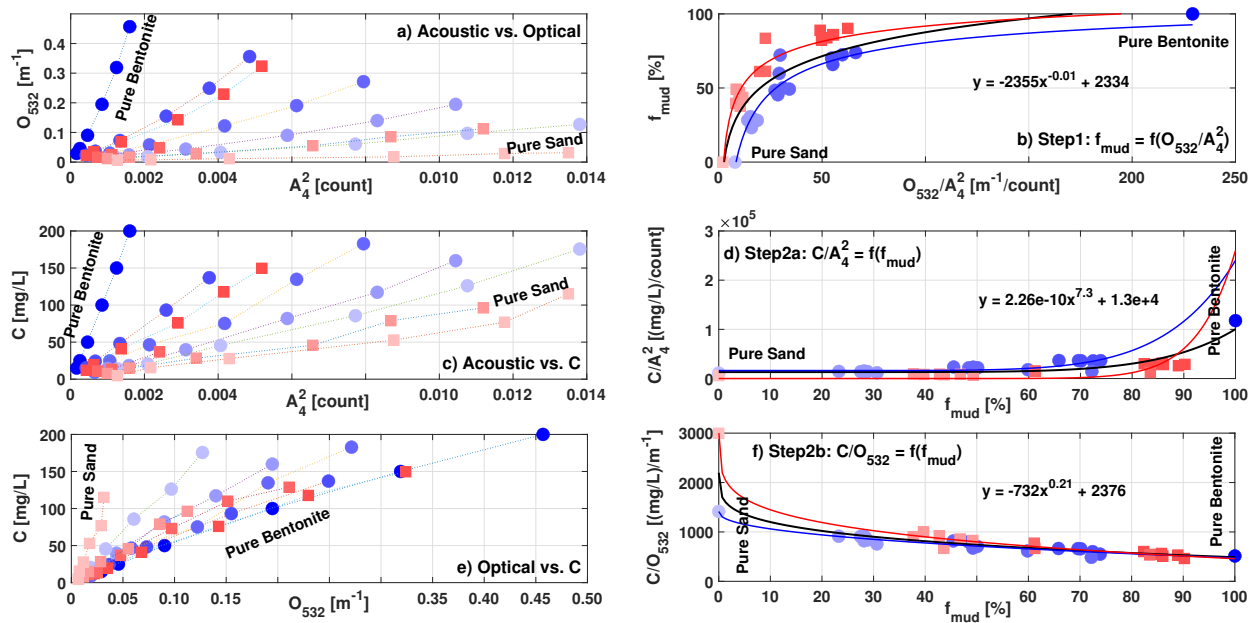


**Figure B11:** Application of SCI method to the optical/acoustic pair of  $O_{532}$  and  $A_4$  with data in C1 (blue), C2 (red) and C12 (black). The reductions of  $f_{mud}$  from 100% to 0% are shown by the darkest color to lightest color. The displayed function are obtained from data set C12.

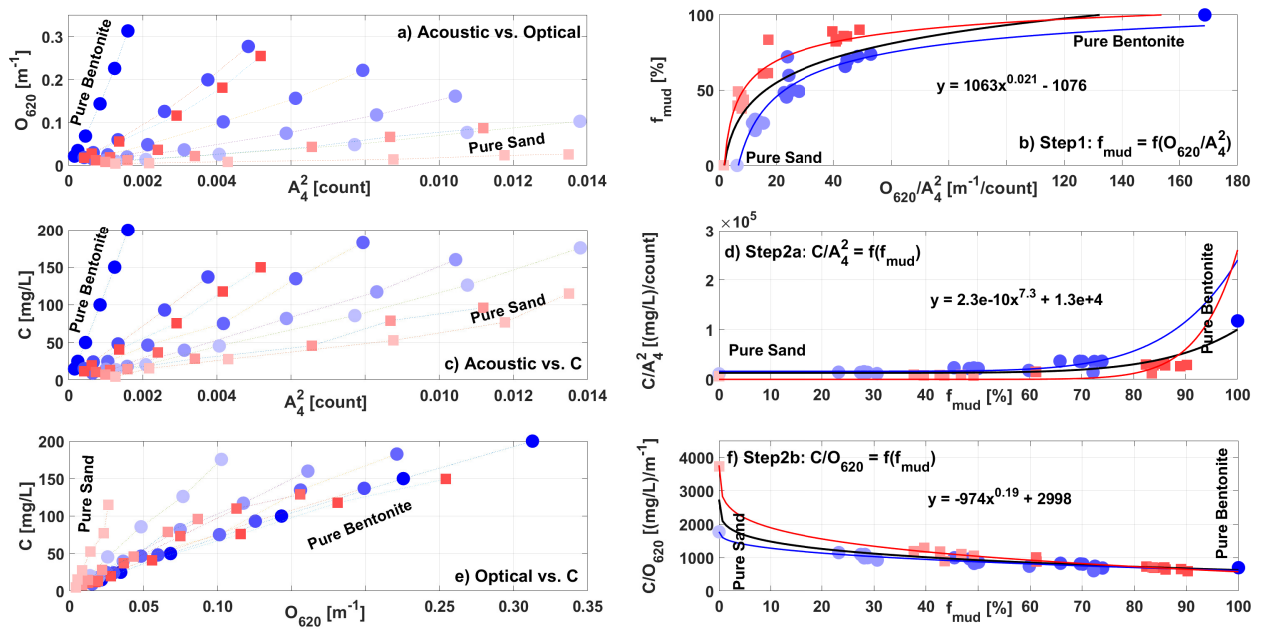


**Figure B12:** Application of SCI method to the optical/acoustic pair of  $O_{620}$  and  $A_4$  with data in C1 (blue), C2 (red) and C12 (black). The reductions of  $f_{mud}$  from 100% to 0% are shown by the darkest color to lightest color. The displayed function are obtained from data set C12.

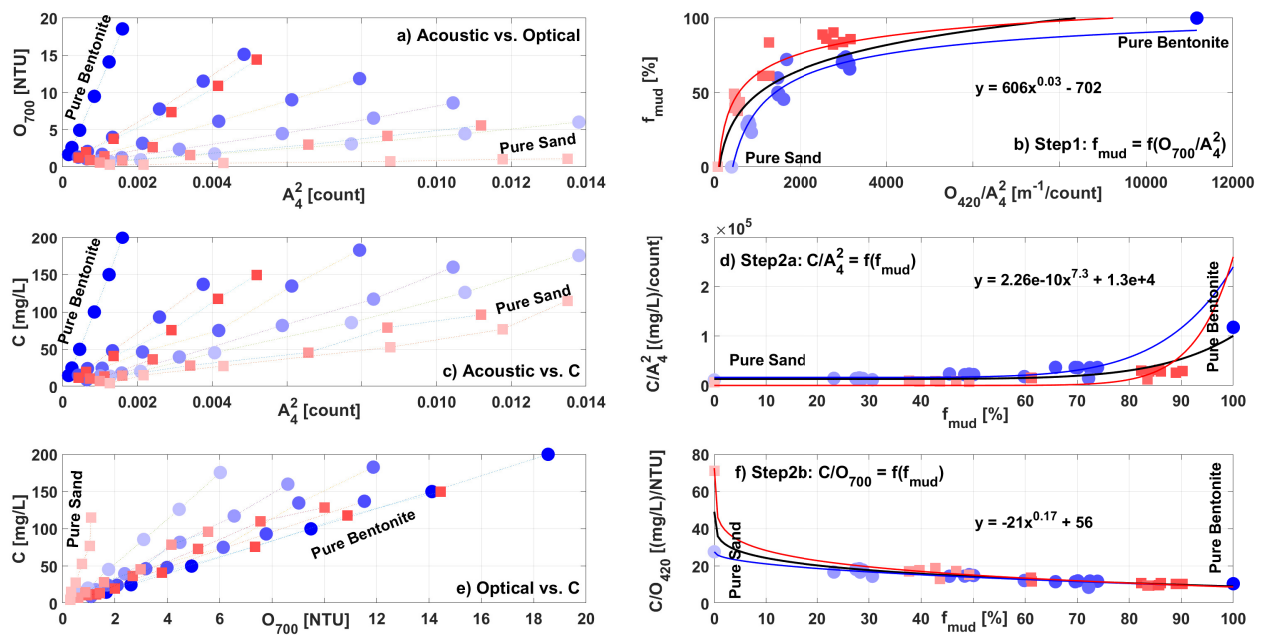


**Figure B13:** Application of SCI method to the optical/acoustic pair of  $O_{700}$  and  $A_4$  with data in C1 (blue), C2 (red) and C12 (black). The reductions of  $f_{mud}$  from 100% to 0% are shown by the darkest color to lightest color. The displayed function are obtained from data set C12.

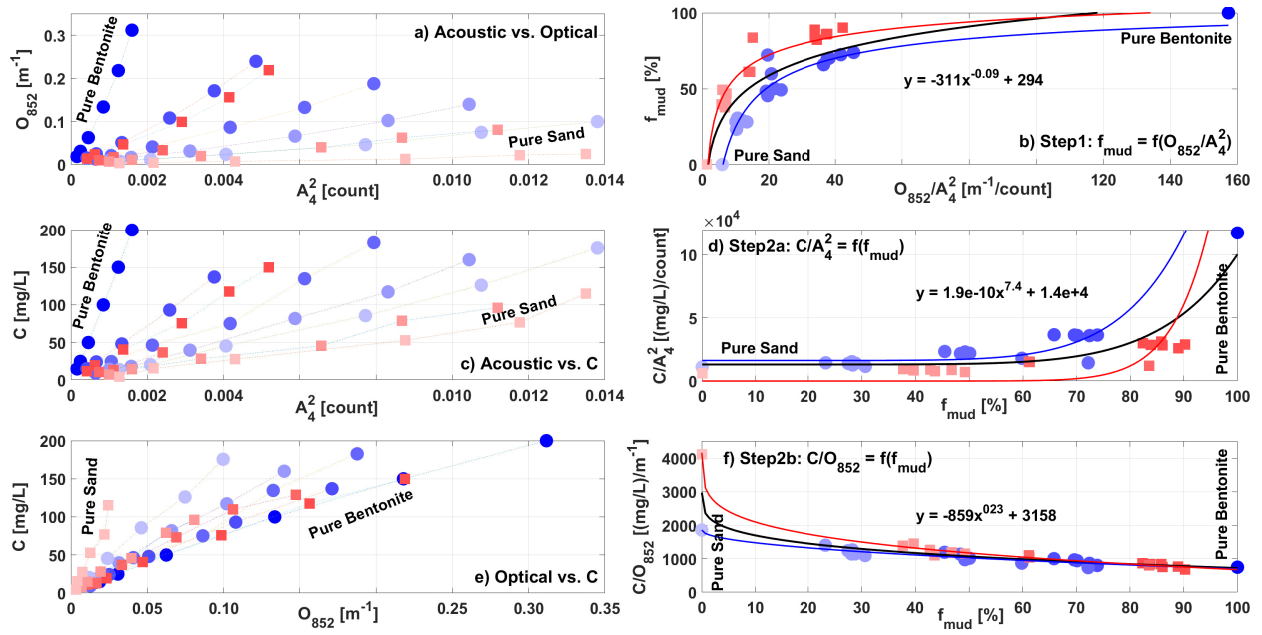


**Figure B14:** Application of SCI method to the optical/acoustic pair of  $O_{852}$  and  $A_4$  with data in C1 (blue), C2 (red) and C12 (black). The reductions of  $f_{mud}$  from 100% to 0% are shown by the darkest color to lightest color. The displayed function are obtained from data set C12.

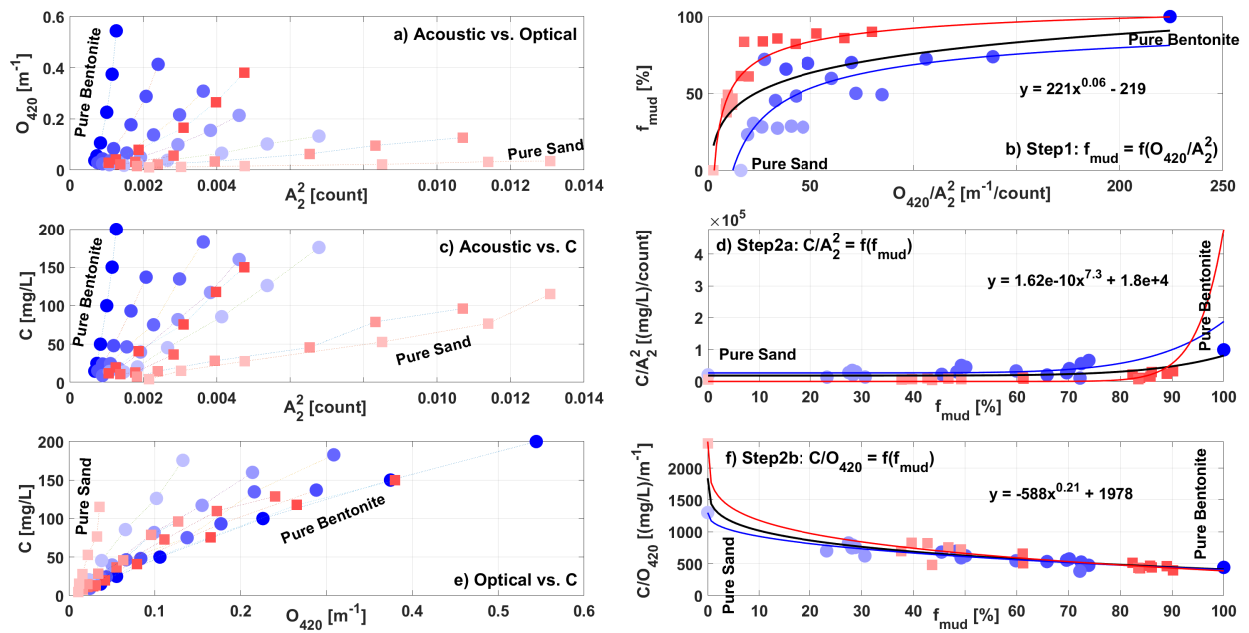


**Figure B15:** Application of SCI method to the optical/acoustic pair of  $O_{420}$  and  $A_2$  with data in C1 (blue), C2 (red) and C12 (black). The reductions of  $f_{mud}$  from 100% to 0% are shown by the darkest color to lightest color. The displayed function are obtained from data set C12.

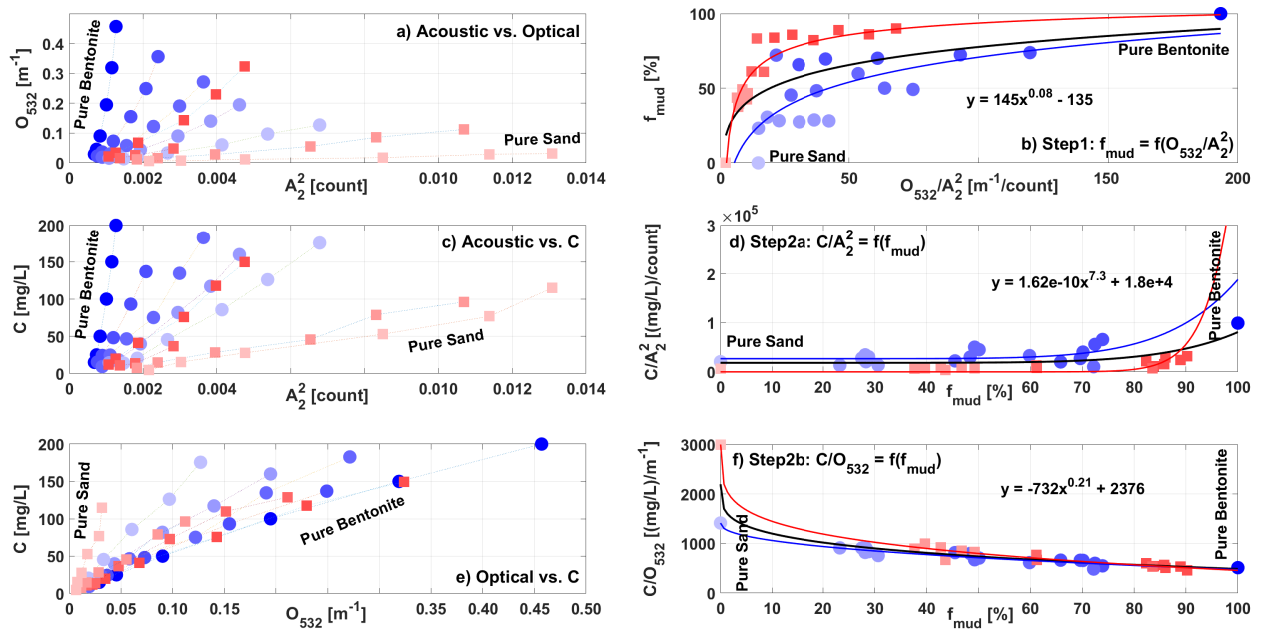


**Figure B16:** Application of SCI method to the optical/acoustic pair of  $O_{532}$  and  $A_2$  with data in C1 (blue), C2 (red) and C12 (black). The reductions of  $f_{mud}$  from 100% to 0% are shown by the darkest color to lightest color. The displayed function are obtained from data set C12.

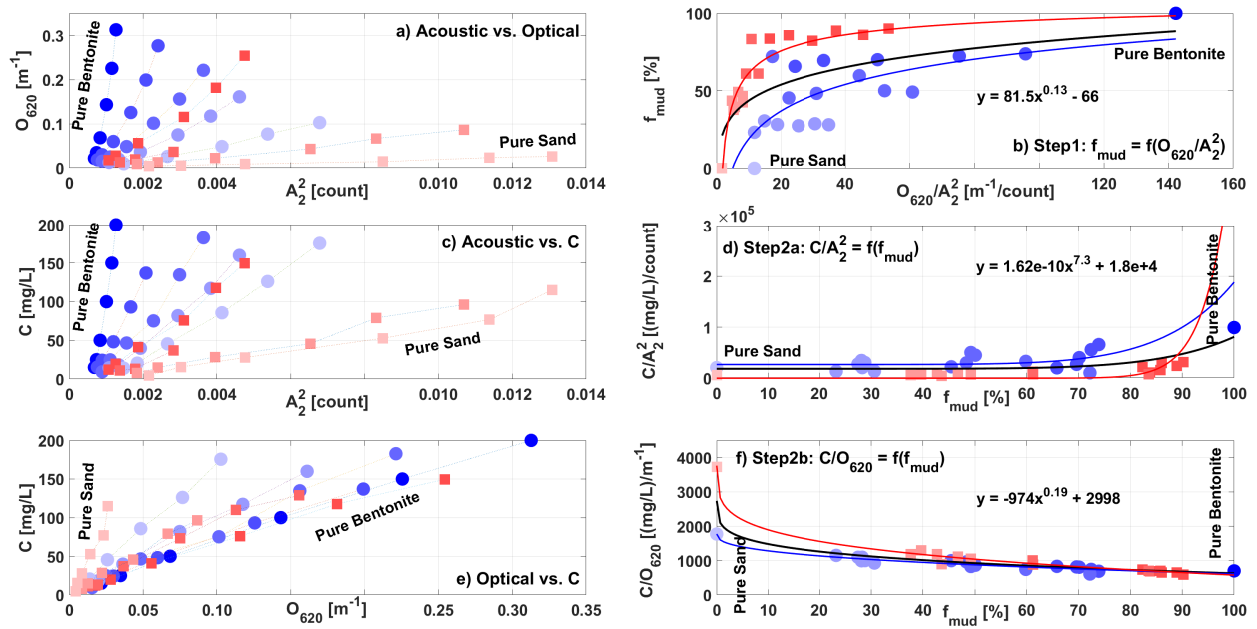


**Figure B17:** Application of SCI method to the optical/acoustic pair of  $O_{620}$  and  $A_2$  with data in C1 (blue), C2 (red) and C12 (black). The reductions of  $f_{mud}$  from 100% to 0% are shown by the darkest color to lightest color. The displayed function are obtained from data set C12.

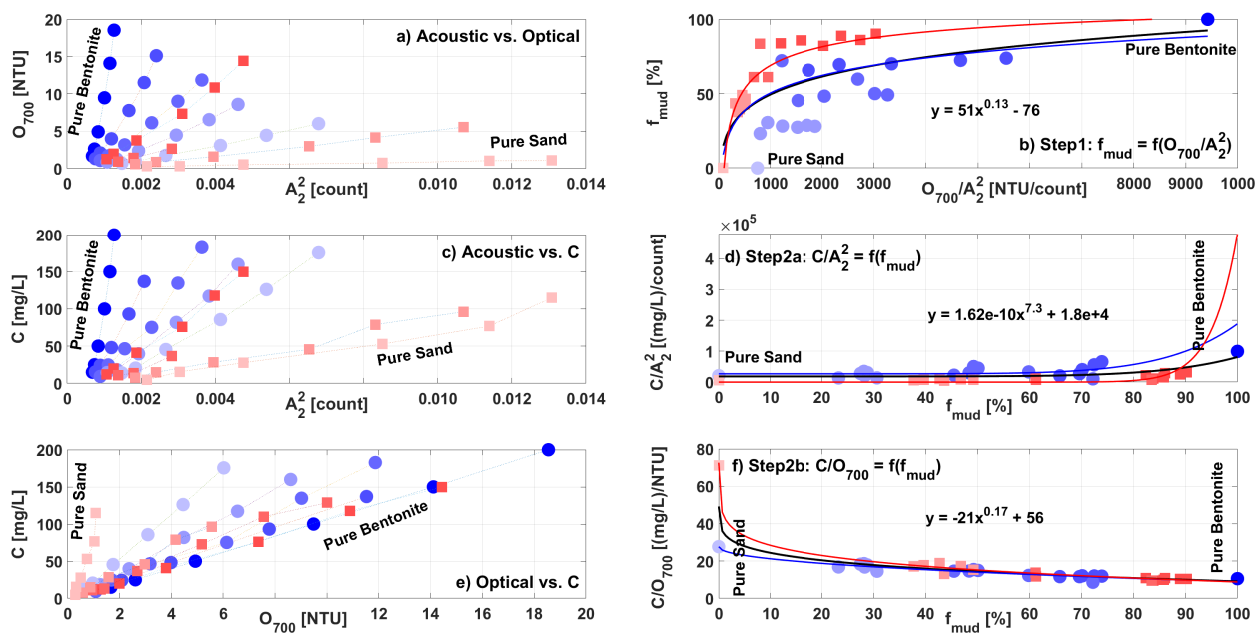


**Figure B18:** Application of SCI method to the optical/acoustic pair of  $O_{700}$  and  $A_2$  with data in C1 (blue), C2 (red) and C12 (black). The reductions of  $f_{mud}$  from 100% to 0% are shown by the darkest color to lightest color. The displayed function are obtained from data set C12.

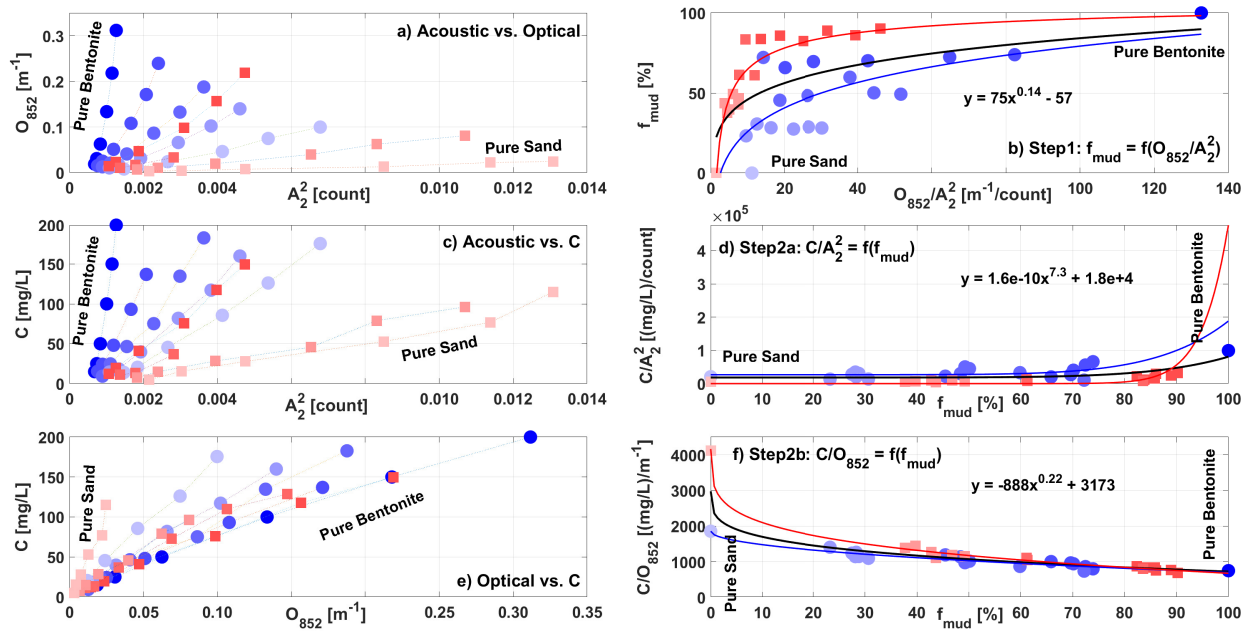


**Figure B19:** Application of SCI method to the optical/acoustic pair of  $O_{852}$  and  $A_2$  with data in C1 (blue), C2 (red) and C12 (black). The reductions of  $f_{mud}$  from 100% to 0% are shown by the darkest color to lightest color. The displayed function are obtained from data set C12.

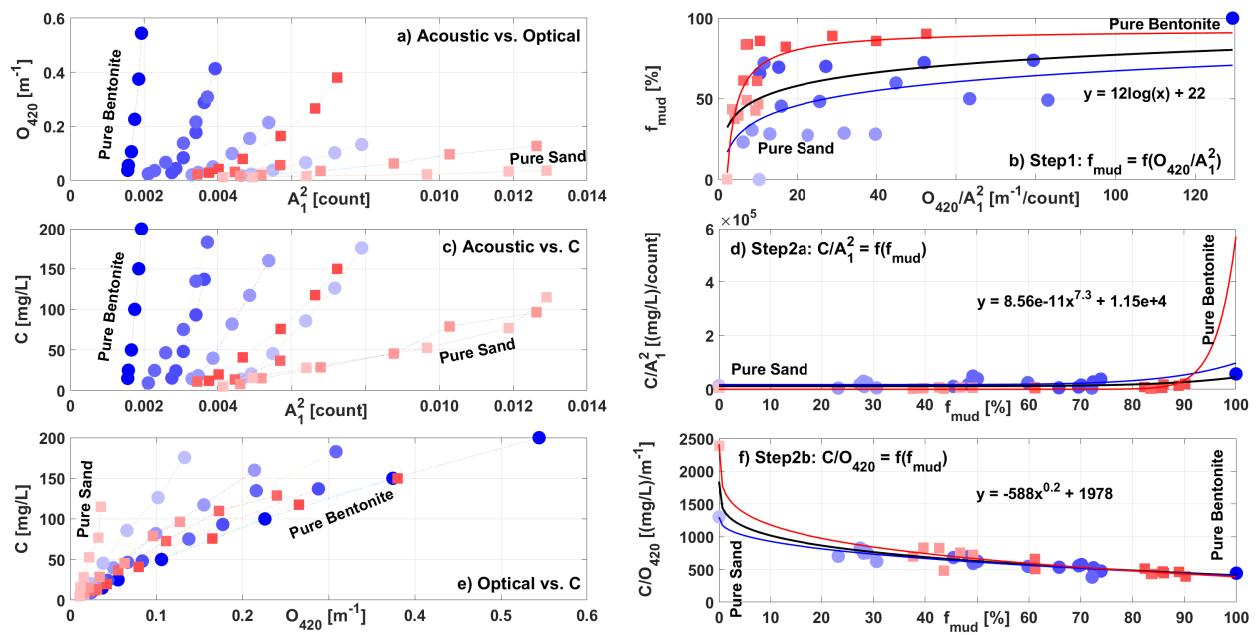


**Figure B20:** Application of SCI method to the optical/acoustic pair of  $O_{420}$  and  $A_1$  with data in C1 (blue), C2 (red) and C12 (black). The reductions of  $f_{mud}$  from 100% to 0% are shown by the darkest color to lightest color. The displayed function are obtained from data set C12.

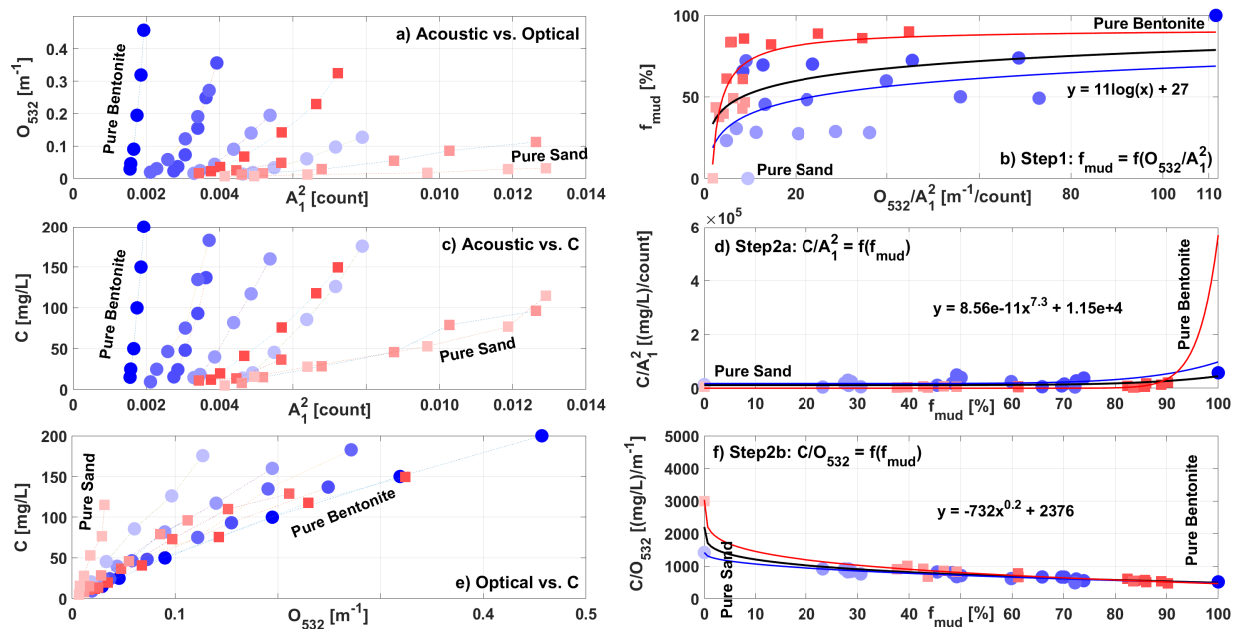


**Figure B21:** Application of SCI method to the optical/acoustic pair of  $O_{532}$  and  $A_1$  with data in C1 (blue), C2 (red) and C12 (black). The reductions of  $f_{mud}$  from 100% to 0% are shown by the darkest color to lightest color. The displayed function are obtained from data set C12.

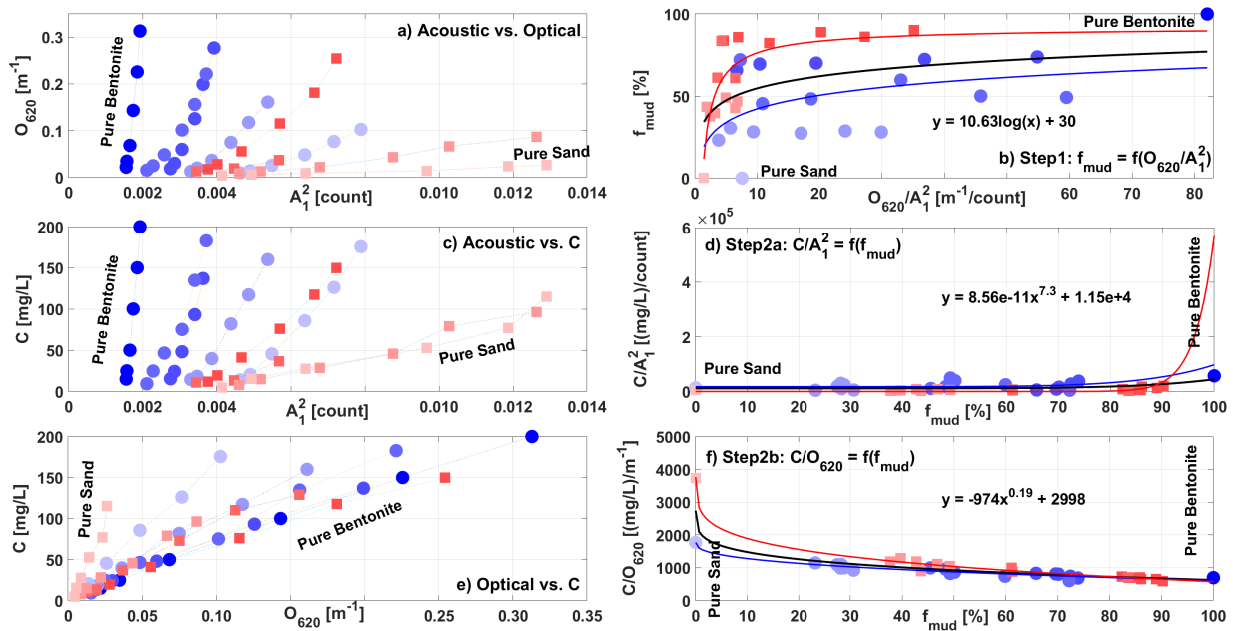


**Figure B22:** Application of SCI method to the optical/acoustic pair of  $O_{620}$  and  $A_1$  with data in C1 (blue), C2 (red) and C12 (black). The reductions of  $f_{mud}$  from 100% to 0% are shown by the darkest color to lightest color. The displayed function are obtained from data set C12.

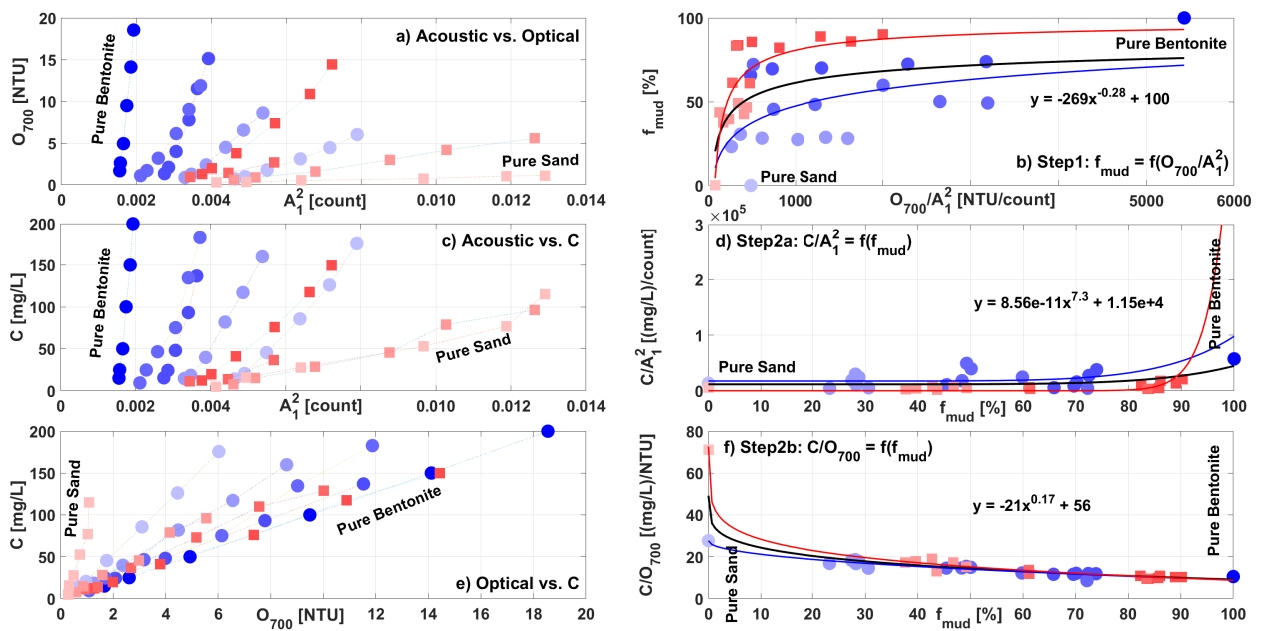


**Figure B23:** Application of SCI method to the optical/acoustic pair of  $O_{700}$  and  $A_1$  with data in C1 (blue), C2 (red) and C12 (black). The reductions of  $f_{mud}$  from 100% to 0% are shown by the darkest color to lightest color. The displayed function are obtained from data set C12.

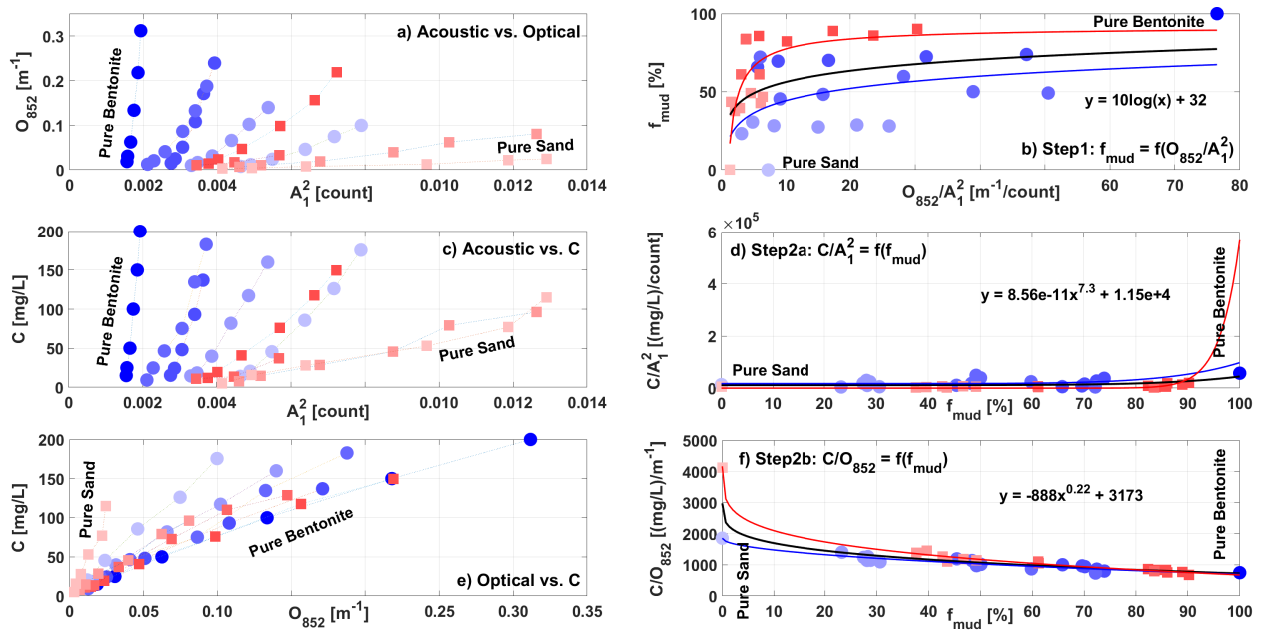


**Figure B24:** Application of SCI method to the optical/acoustic pair of  $O_{852}$  and  $A_1$  with data in C1 (blue), C2 (red) and C12 (black). The reductions of  $f_{mud}$  from 100% to 0% are shown by the darkest color to lightest color. The displayed function are obtained from data set C12.

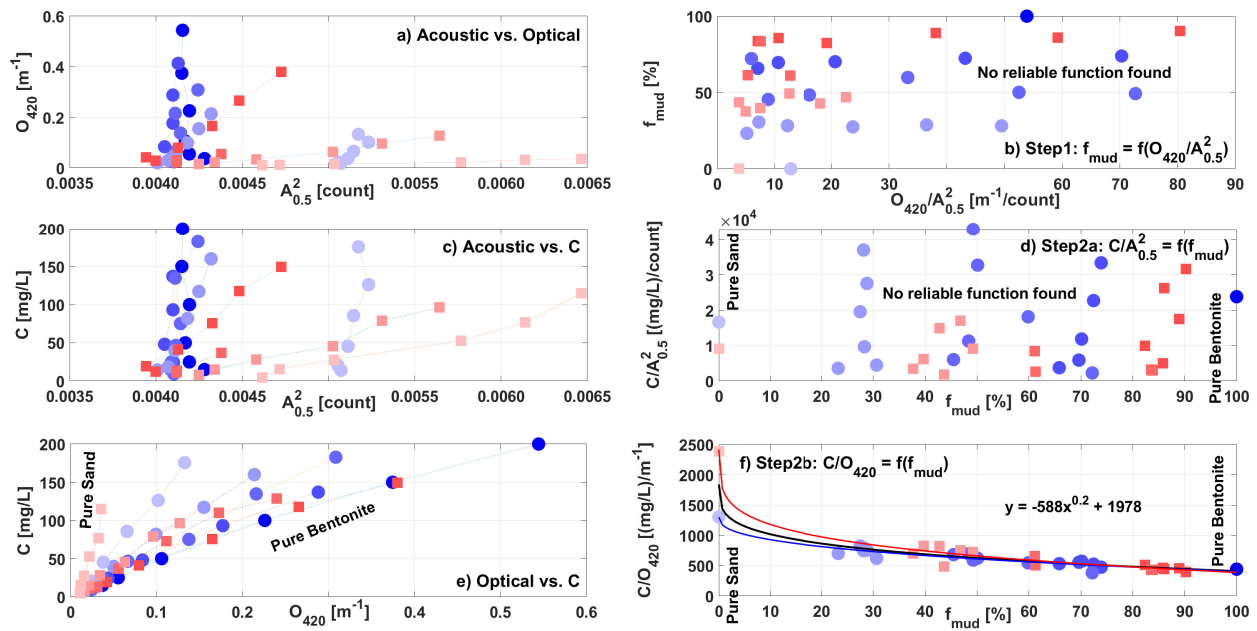


**Figure B25:** Application of SCI method to the optical/acoustic pair of  $O_{420}$  and  $A_{0.5}$  with data in C1 (blue), C2 (red) and C12 (black). The reductions of  $f_{mud}$  from 100% to 0% are shown by the darkest color to lightest color. The displayed function are obtained from data set C12.

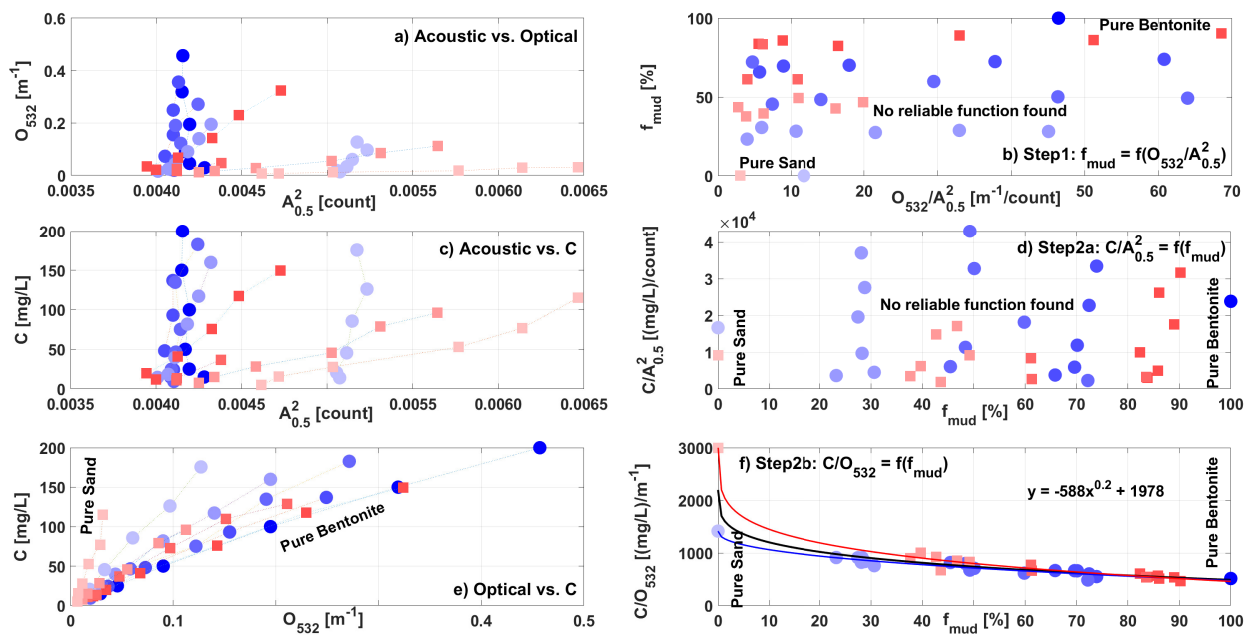


**Figure B26:** Application of SCI method to the optical/acoustic pair of  $O_{532}$  and  $A_{0.5}$  with data in C1 (blue), C2 (red) and C12 (black). The reductions of  $f_{mud}$  from 100% to 0% are shown by the darkest color to lightest color. The displayed function are obtained from data set C12.

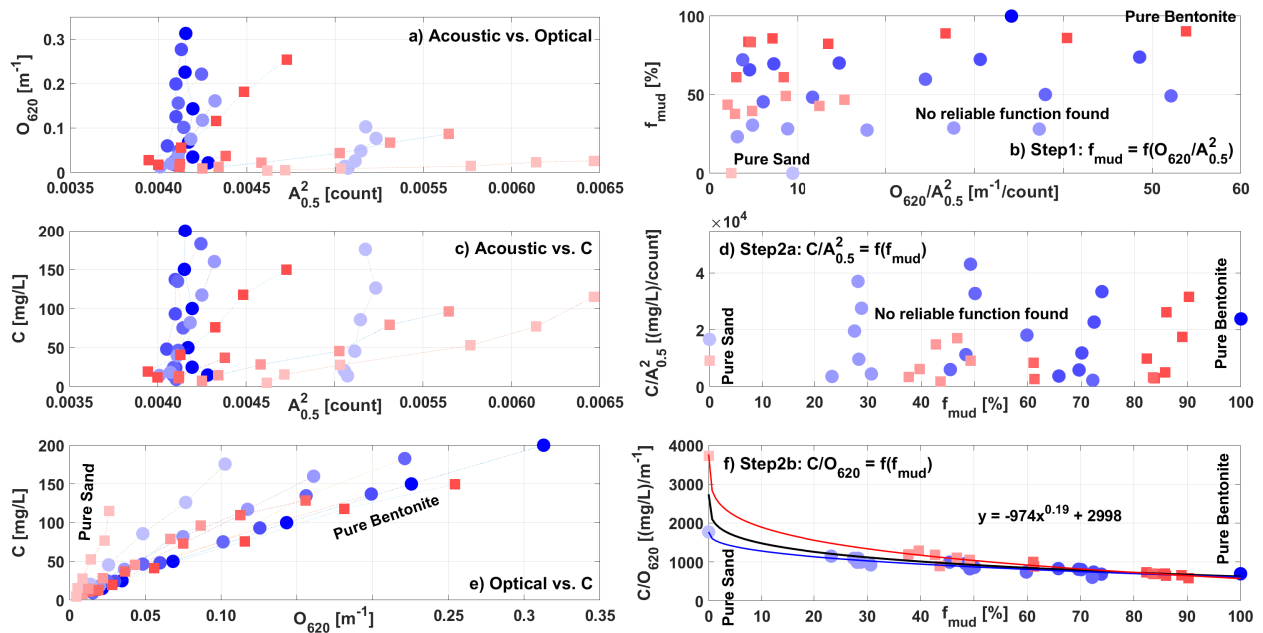


**Figure B27:** Application of SCI method to the optical/acoustic pair of  $O_{620}$  and  $A_{0.5}$  with data in C1 (blue), C2 (red) and C12 (black). The reductions of  $f_{mud}$  from 100% to 0% are shown by the darkest color to lightest color. The displayed function are obtained from data set C12.

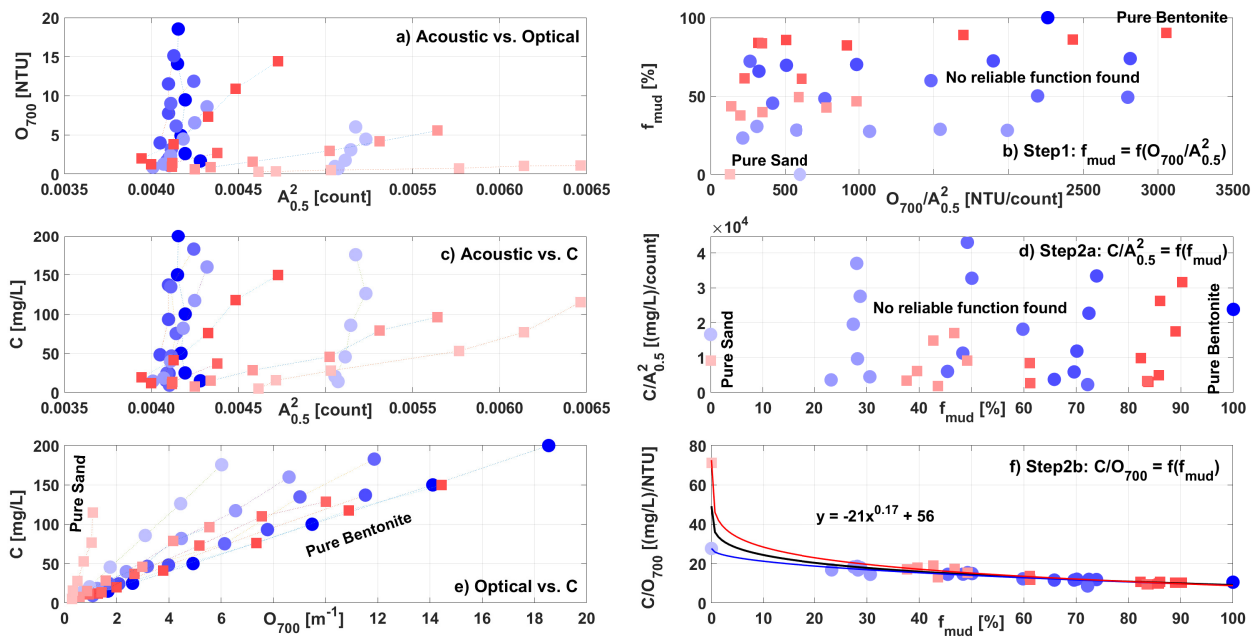


**Figure B28:** Application of SCI method to the optical/acoustic pair of  $O_{700}$  and  $A_{0.5}$  with data in C1 (blue), C2 (red) and C12 (black). The reductions of  $f_{mud}$  from 100% to 0% are shown by the darkest color to lightest color. The displayed function are obtained from data set C12.

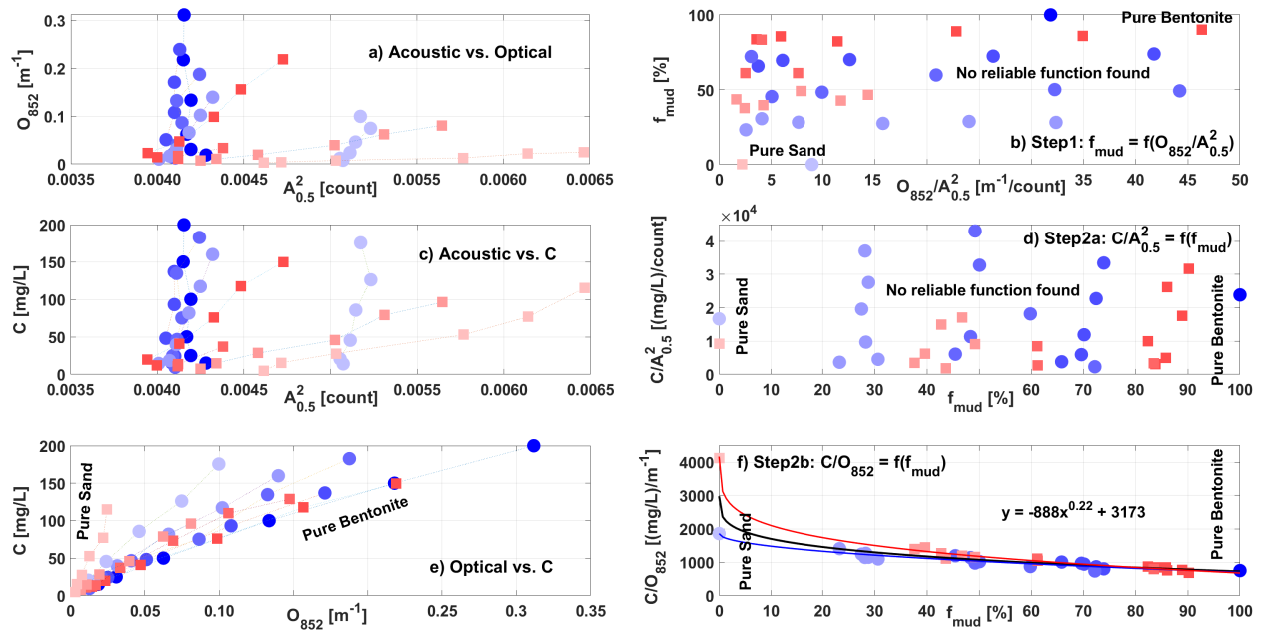


**Figure B29:** Application of SCI method to the optical/acoustic pair of  $O_{852}$  and  $A_{0.5}$  with data in C1 (blue), C2 (red) and C12 (black). The reductions of  $f_{mud}$  from 100% to 0% are shown by the darkest color to lightest color. The displayed function are obtained from data set C12.

447 **References**

448 Aquatec Subsea Ltd (2012). Application Note AN4 - inversion technique. AN4Rev1.0.

449 Bux, J., Peakall, J., Rice, H. P., Manga, M. S., Biggs, S., and Hunter, T. N. (2019). Measurement  
450 and density normalisation of acoustic attenuation and backscattering constants of arbitrary  
451 suspensions within the rayleigh scattering regime. *Applied Acoustic*, 146:9 – 22.

452 Chmiel, O., Baselt, I., and Malcherek, A. (2018). Applicability of acoustic concentration mea-  
453 surements in suspensions of artificial and natural sediments using an acoustic doppler ve-  
454 locimeter. *Acoustics*, 1(1):59–77.

455 Downing, J. (2006). Twenty-five years with OBS sensors: The good, the bad, and the ugly. *Con-  
456 tinental Shelf Research*, 26(17):2299–2318.

457 Doxaran, D., Leymarie, E., Nechad, B., Dogliotti, A., Ruddick, K., Gernez, P., and Knaeps, E.  
458 (2016). Improved correction methods for field measurements of particulate light backscat-  
459 tering in turbid waters. *Optics Express*, 24(4):3615.

460 Druine, F., Verney, R., Deloffre, J., Lemoine, J., Chapalain, M., Landemaine, V., and Lafite, R.  
461 (2018). In situ high frequency long term measurements of suspended sediment concentra-  
462 tion in turbid estuarine system (seine estuary, france): Optical turbidity sensors response to  
463 suspended sediment characteristics. *Marine Geology*, 400:24–37.

464 Fettweis, M., Riethmüller, R., Verney, R., Becker, M., Backers, J., Baeye, M., Chapalain, M.,  
465 Claeys, S., Claus, J., Cox, T., Deloffre, J., Depreiter, D., Druine, F., Flöser, G., Grünler, S., Jourdin,  
466 F., Lafite, R., Nauw, J., Nechad, B., Röttgers, R., Sottolichio, A., Van Engeland, T., Vanhaverbeke,  
467 W., and Vereecken, H. (2019). Uncertainties associated with in situ high-frequency long-term  
468 observations of suspended particulate matter concentration using optical and acoustic sen-  
469 sors. *Progress in Oceanography*, 178:102162.

470 Haalboom, S., de Stigter, H., Duineveld, G., van Haren, H., Reichart, G. J., and Mienis, F. (2021).  
471 Suspended particulate matter in a submarine canyon Whittard Canyon, Bay of Biscay, NE  
472 Atlantic Ocean : Assessment of commonly used instruments to record turbidity. *Marine Ge-*  
473 *ology*, 434:106439.

474 Hoitink, A. and Hoekstra, P. (2005). Observation of suspended sediment from adcp and obs  
475 measurements in a mud-dominated environment. *Coastal Engineering*, 52(2):103–118.

476 Livsey, D. N., Turner, R. D. R., and Grace, P. R. (2023). Combining optical and acoustic backscat-  
477 ter measurements for monitoring of fine suspended-sediment concentration under changes  
478 in particle size and density. *Water Resources Research*, 59(8):1–20.

479 Lynch, J. F., Irish, J. D., Sherwood, C. R., and Agrawal, Y. C. (1994). Determining suspended  
480 sediment particle size information from acoustical and optical backscatter measurements.  
481 *Continental Shelf Research*, 14(10-11):1139–1165.

482 Moate, B. D. and Thorne, P. D. (2009). Measurements and inversion of acoustic scattering from  
483 suspensions having broad size distributions. *Journal of the Acoustical Society of America*,  
484 126(6):2905 – 2917.

485 Moura, M. G., Quaresma, V. S., Bastos, A. C., and Veronez, P. (2011). Field observations of SPM  
486 using ADV, ADP, and OBS in a shallow estuarine system with low SPM concentration-Vitória  
487 Bay, SE Brazil. *Ocean Dynamics*, 61(2-3):273–283.

488 Pearson, S. G., Verney, R., van Prooijen, B. C., Tran, D., Hendriks, E. C., Jacquet, M., and Wang,  
489 Z. B. (2021). Characterizing the composition of sand and mud suspensions in coastal and es-  
490 tuarine environments using combined optical and acoustic measurements. *Journal of Geo-*  
491 *physical Research : Oceans*, 126:e2021JC017354.

492 Sahin, C., Verney, R., Sheremet, A., and Voulgaris, G. (2017). Acoustic backscatter by suspended  
493 cohesive sediments : Field observations, seine estuary, france. *Continental Shelf Research*,  
494 134:39–51.

- 495 Salehi, M. and Strom, K. (2011). Using velocimeter signal to noise ratio as a surrogate measure  
496 of suspended mud concentration. *Continental Shelf Research*, 31(9):1020–1032.
- 497 Slade, W. H., Boss, E., and Russo, C. (2011). Effects of particle aggregation and disaggregation  
498 on their inherent optical properties. *Optics Express*, 19(9):7945–7959.
- 499 Sutherland, T. F., Lane, P. M., Amos, C. L., and Downing, J. (2000). The calibration of opti-  
500 cal backscatter sensors for suspended sediment of varying darkness levels. *Marine Geology*,  
501 162(2-4):587–597.
- 502 Thorne, P. D. and Hurther, D. (2014). An overview on the use of backscattered sound for measur-  
503 ing suspended particle size and concentration profiles in non-cohesive inorganic sediment  
504 transport studies. *Continental Shelf Research*, 73:97–118.
- 505 Thorne, P. D., Lichtman, I. D., and Hurther, D. (2021). Acoustic scattering characteristics and  
506 inversions for suspended concentration and particle size above mixed sand and mud beds.  
507 *Continental Shelf Research*, 214:104320.
- 508 Tran, D., Jacquet, M., Pearson, S., and Verney, R. (2021). Investigating suspended particulate  
509 matters from multi-wavelength optical and multi-frequency acoustic measurements. *EGU*  
510 *2021*, page 13022.